Geomorphology 465 (2024) 109400

Contents lists available at ScienceDirect

Geomorphology

journal homepage: www.journals.elsevier.com/geomorphology

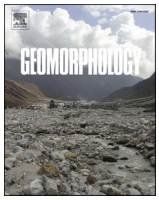

Morphometric analysis of monogenetic volcanoes in the Garrotxa Volcanic Field, Iberian Peninsula

Dario Pedrazzi [a,*], Gabor Kereszturi [b], Adelina Geyer [a], Xavier Bolós [a], Jordi Granell [c], Llorenç Planagumà [d], Joan Martí [e], Daniela Cerda [a]

[a] Geoscience Barcelona (GEO3BCN), CSIC, Lluís Solé Sabarís s/n, 08028 Barcelona, Spain
[b] Volcanic Risk Solutions, School of Agriculture and Environment, Massey University, Palmerston North, New Zealand
[c] Department of Mineralogy, Petrology and Applied Geology, University of Barcelona, Spain
[d] Geonat, Geology & Environment, 17800 Olot, Spain
[e] Dep. of Geosciences, IDAEA-CSIC Institute of Environmental Assessment and Water Research, Jordi Girona St., 18-26, Spain

ARTICLE INFO

Keywords:
Tuff ring
Scoria cone
Cinder cones
Phreatomagmatic
Digital Elevation Model
Cenozoic Rift
Morphometry

ABSTRACT

The Garrotxa Volcanic Field is situated in the northeast region of the Iberian Peninsula. It represents the most recent volcanic area within the Catalan Volcanic Zone, which is one of the volcanic provinces of the European Rift System, featuring over 50 dispersed eruptive vents.

This study presents a comprehensive morphometric analysis of volcanic edifices, aiming to enhance our understanding of both volcanostratigraphy and the geomorphology of landforms within the Garrotxa Volcanic Field. Our methodology involved extensive fieldwork and detailed analysis of Digital Elevation Models (DEMs) to precisely determine the spatial distribution and morphometric parameters of the best-preserved volcanic structures in the area. The Garrotxa Volcanic Field exhibits an uneven spatial distribution of various volcanic landforms, with approximately 50 % comprising magmatic cones, primarily formed through Strombolian eruptions. The remaining 50 % is evenly divided between magmatic-phreatomagmatic volcanoes and phreatomagmatic tuff rings-maars. The morphometric characteristics of the three genetic types overlap significantly, showing no clear differences, although a few distinctions can sometimes be identified.

The Garrotxa Volcanic Field displays a variety of eruption styles: 46 % of the identified eruptive sequences begin with phreatomagmatic activity, while 54 % start with predominantly magmatic explosive activity. Most eruptions show a transition through different phases.

Data also indicate that the morphometric variability at the Garrotxa Volcanic Field stems from differences in the properties of pyroclastic sequences, resulting from their diverse eruption styles, as well as pre- and post-eruptive factors. Consequently, the results of the morphometric analysis are deemed insufficient for establishing a reliable chronology for the Garrotxa Volcanic Field.

1. Introduction

Monogenetic volcanoes are among the most common landforms on Earth (Wood, 1979) and are often associated with volcanic fields (Valentine and Connor, 2015). From a geomorphological point of view, monogenetic volcanoes are traditionally considered to have simple geometry due to their small size and volume, between 0.0001 and 1 km^3 (Vespermann and Schmincke, 2000). These volcanoes reflect various eruption styles, including magmatic and phreatomagmatic fragmentation, and can be classified by their surface morphotypes into spatter cones, scoria cones, domes, tuff rings/maars, and tuff cones (Kereszturi and Németh, 2012; Kurszlaukis and Lorenz, 2017; Murcia and Németh, 2020).

Scoria cones primarily consist of granular, lapilli-to-block/bomb grain size populations (Guilbaud et al., 2011; Delcamp et al., 2014; Kereszturi and Németh, 2016), allowing the dry and cohesionless particles to maintain a maximum angle of repose of 32–34° (McGetchin et al., 1974; Wood, 1980b). In contrast, deposits within tuff cones and tuff rings are often very cohesive and fine-grained, resulting from the emplacement by fallout or density currents of wet, poorly sorted ejecta

* Corresponding author.
E-mail address: dpedrazzi@geo3bcn.csic.es (D. Pedrazzi).

https://doi.org/10.1016/j.geomorph.2024.109400
Received 29 August 2023; Received in revised form 19 July 2024; Accepted 23 August 2024
Available online 29 August 2024

composed of juvenile clasts and variable amounts of accidental clasts (Vespermann and Schmincke, 2000; Valentine and Connor, 2015). Consequently, the initial volcano geomorphology is strongly controlled by eruptive processes and depositional mechanisms and granulometric properties (Thouret, 1999; Kereszturi and Németh, 2012).

Scoria cones are the most abundant landforms in the Garrotxa Volcanic Field (GVF; Fig. 1) with subordinate maars and tuff rings (Martí et al., 2011). The GVF has experienced intermittent volcanic activity starting approximately 700 ka, forming over 50 volcanic vents. The last eruption took place 11 to 13 ky ago at the Croscat volcano (Martí et al., 2011; Puiguriguer et al., 2012; Bolós et al., 2014b).

Numerous investigations have been carried out in the GVF, primarily

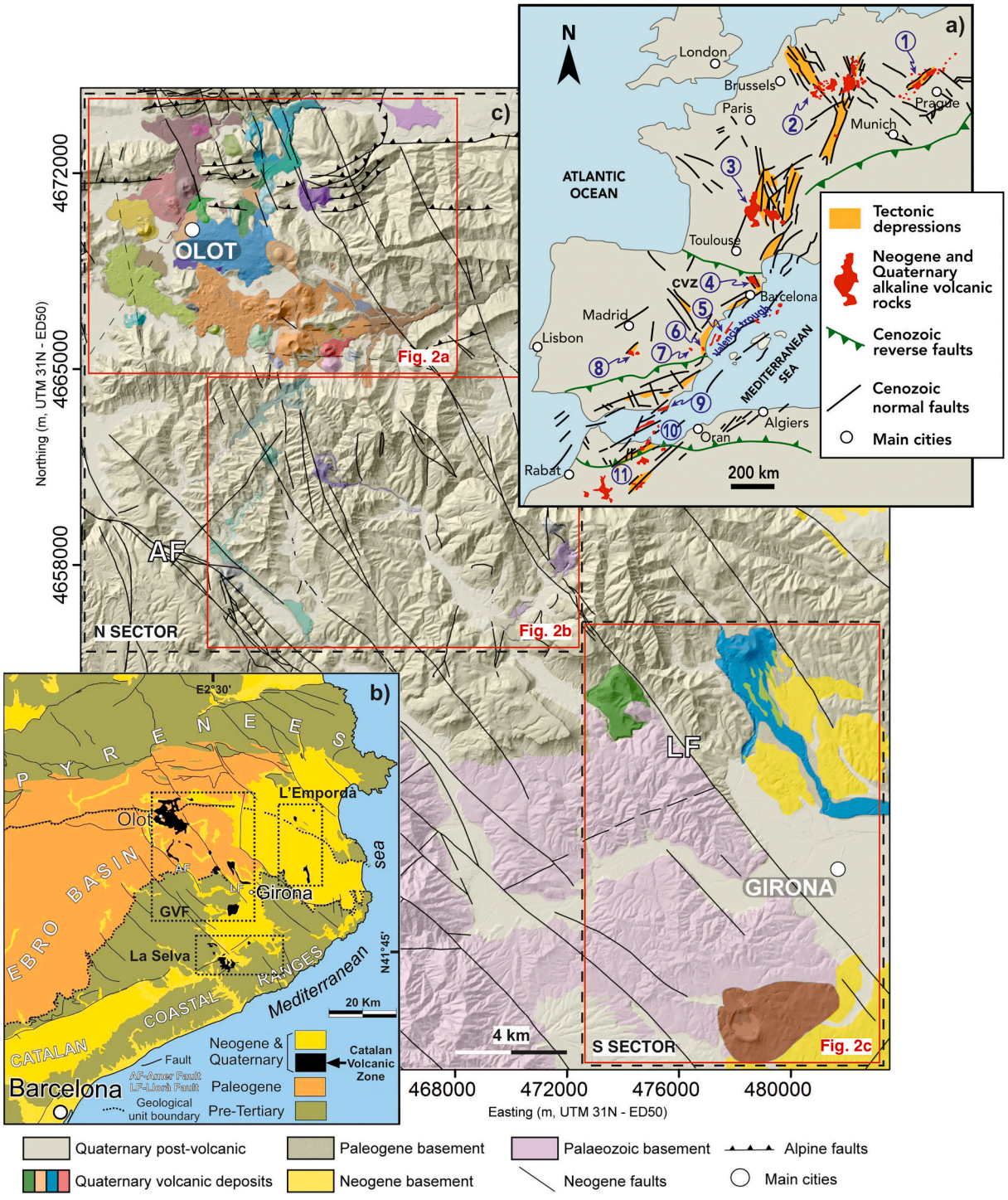

Fig. 1. a) Location of the Western European Rift and distribution of Neogene-Quaternary volcanism: 1: Bohemian Massif, Czech Republic; 2: Rhenish Graben, Germany; 3: Massif Central, France; 4: Catalan Volcanic Zone (CVZ), Spain; 5: Columbretes Islands, Spain; 6: Picasent, Spain; 7: Cofrentes, Spain; 8: Calatrava Volcanic Field, Spain; 9: Cabo de Gata, Spain; 10: Alborán submarine volcanoes, Spain; 11: Eastern Rif and Atlas volcanism, Spain, Morocco (Martí and Bolós, 2019); b) geological map of the CVZ and location of L'Empordà, La Selva and GVF, outlined in black dotted rectangles. c) simplified geological map of GVF, highlighting the northern and southern sectors, outlined in black dotted rectangles (modified from Bolós et al., 2015). Subzones inside red rectangles refer to Fig. 2. LF = Llorà Fault, AF = Amer Fault.

focusing on its petrology and geochemistry (e.g., Araña et al., 1983; López Ruiz and Rodríguez Badiola, 1985; Martí et al., 1992; Neumann et al., 1999; Cebrià et al., 2000; Galán et al., 2016; Miranda-Muruzábal et al., 2024). Over the past decades, significant efforts have been made to characterize the physical volcanology of these landforms along with their geochronological data and the associated hazards (e.g., Martí et al., 2011; Pedrazzi et al., 2014, 2016, 2022; Bolós et al., 2015; Bartolini et al., 2015). A recent study conducted by Iriarte et al. (2023) analyzed sedimentary lacustrine sediments from a drill core, revealing multiple ash layers dating back from 13.5 to 8.3 ky cal BP. Furthermore, preliminary works on geomorphology have been conducted (Roqué et al., 2014; Bolós et al., 2015), although a more comprehensive study had not been carried out until now. Therefore, this work provides a new catalogue of volcanoes, including eruptive and geomorphic parameters of monogenetic volcanoes in the GVF, through morphometric analysis supported by geophysics and field-based studies (Barde-Cabusson et al., 2013, 2014; Bolós et al., 2012, Bolós et al., 2014a, b, Bolós et al., 2015; Martí et al., 2011, 2017; Roqué et al., 2014; Pedrazzi et al., 2014, 2016, 2022; Planagumà et al., 2023).

Morphometric analysis has been applied since the 1970s for the study of monogenetic volcanoes, particularly focusing on scoria cones (e.g., Porter, 1972; McGetchin et al., 1974; Wood, 1980a, 1980b; Dohrenwend et al., 1986; Tibaldi, 1995; Dóniz-Páez, 2015; Pedersen, 2016; Haag et al., 2019; Grosse et al., 2020; Aguilera et al., 2022). The latter, in particular, offer an ideal target for comparative morphometric studies (Kervyn et al., 2012; Kereszturi et al., 2013; Favalli et al., 2009; Zarazúa-Carbajal et al., 2024). Recent investigations have demonstrated that scoria cone morphology and their spatial distribution can reflect volcanic field dynamics and controlling factors, such as structural control, eruption style and climate (e.g., Bemis and Ferencz, 2017; Ben-Asher et al., 2017; Pedersen et al., 2020; Smellie et al., 2023). Furthermore, morphometric analysis has been, also, widely used for establishing control over the geochronology and evolution of volcanic fields (e.g., Bemis et al., 2011; Fornaciai et al., 2012; Kereszturi et al., 2012, Kereszturi et al., 2013; Dóniz-Páez, 2015; Bemis and Ferencz, 2017; Schonwalder-Angel et al., 2018; Nieto-Torres and Del Pozzo, 2019; Pedrazzi et al., 2020; Zarazúa-Carbajal et al., 2024).

Here, we present a comprehensive morphometric analysis of the best-preserved volcanic cones within the GVF. This study utilizes morphometric parameters, including cone (W_{co}) and crater (W_{cr}) mean diameters, as well as cone maximum height (H_{max}), maximum crater depth (D_{crmax}) and external slope of the cone (S_{mean}) to integrate geomorphology data with physical volcanology and volcano-stratigraphy (e.g., Pedrazzi et al., 2014, 2016, 2022; Martí et al., 2017; Planagumà et al., 2023). The aim is to assess the geomorphic evolution of these monogenetic volcanoes, related dynamics and controlling factors, as well as the spatial distribution inside the GVF. This is the key to refine, in the future, the short- and long-term volcanic hazards within the GVF.

2. Geological setting

The GVF (0.7–0.01 Ma) is located in the NE Iberian Peninsula (Fig. 1a). Alongside La Selva (7.9–1.7 Ma) and L'Empordà (>12–8 Ma) volcanic fields (Fig. 1b), it belongs to the Catalan Volcanic Zone (CVZ), which is one of the alkaline volcanic provinces of the European Cenozoic Rift System (Araña et al., 1983; Martí et al., 1992; Fig. 1a). This rift system evolved in the Alpine foreland during late Eocene to recent times, coinciding with the main and late Alpine orogenic phases (Ziegler, 1992). Volcanic activity in the GVF occurred intermittently throughout the Quaternary, spanning from 700 ky to approximately 11 ky. Eruptive events took place, on average, every 10 to 30 ky (Martí et al., 2017).

Most of the cones formed during brief eruptions associated with widely distributed fractures of limited lateral extent (Martí et al., 2011). These eruptions involved alternating Strombolian and phreatomagmatic episodes, resulting in complex stratigraphic sequences comprising a diverse range of pyroclastic deposits including fallout and dense and dilute Pyroclastic Density Currents (PDCs) (Martí and Mallarach, 1987; Martí et al., 1986, 2011, 2017; Di Traglia et al., 2009; Gisbert et al., 2009; Bolós et al., 2014a, 2014b; Cimarelli et al., 2013; Pedrazzi et al., 2014, 2016, 2022).

The GVF encompasses about 50 volcanic edifices (Figs. 1c and 2) and covers an area of roughly 600 km^2. It is located between the cities of Olot and Girona (Fig. 1b) and is laterally limited by two main NW–SE fault systems: the Llorà Fault (LF) to the east and the Amer Fault (AF) to the west (Bolós et al., 2015) (Fig. 1b,c). The vent density is notably higher within a folded Eocene basement, between the towns of Olot and Santa Pau, in the northern part of the GVF, corresponding to the Fluvià river basin (Fig. 1c). Volcanoes in the southern sector of the volcanic field are located on a Palaeozoic-Neogene basement that coincides with the Ter River basin (Fig. 1c) (Martí et al., 2011).

3. Methods

3.1. Morphological and morphometric analysis

The morphometric parameters of monogenetic edifices (Fig. 3 and Table 1) were quantified using a Light Detection and Ranging (LiDAR) derived Digital Elevation Model (DEM) with 2 m resolution. The point cloud data were collected between 2008 and 2011 by the Institut Cartogràfic i Geològic de Catalunya (ICGC) (https://www.icgc.cat/Descarregues/Elevacions/Dades-lidar).

These measurements were complemented by geological maps of Catalonia at a scale of 1:25,000 from the ICGC (MGC25M). The specific sheet numbers used include Riudaura 256-2-2, Olot 257-1-2, Les Preses 294-2-1, Santa Pau 295-1-1, Banyoles 295-2-1, Amer 295-1-2, Canet d'Àdri 295-2-2, Sarrià de Ter 296-1-2, Salt 333-2-1 and Santa Coloma de Farners 333-2-2. Additionally, the volcanological map of the La Garrotxa Volcanic Zone Natural Park at a scale of 1:25,000 (Losantos et al., 2007) and the stratigraphic map by Bolós et al. (2014a, b) were also utilized.

This research builds upon previous works carried out by Roqué et al. (2014) and Bolós et al. (2015). We conducted a more comprehensive study of the volcanic landforms, extracting a more complete set of morphometric parameters (Table 1 and Supp. Material 1) and performing statistical analyses on the inner and outer flanks (Supp. Material 2–4), as well as on the spatial distribution and density (Figs. 11 and 12).

Each edifice (N) within the GVF was identified, along with their corresponding coordinates (UTM WGS84, zone 31 N) and geographic locations (the closest city or toponym; e.g., Olot). Additionally, we reported absolute radiometric ages (if available) and quality rating of each landform [*low* - only a small portion of the cone is preserved; *medium* - at least half or more of the cone is preserved; *high* - the cone is completely (or almost completely) preserved].

Subsequently, a morphometric analysis (Fig. 3) was conducted exclusively on the best-preserved cones (43) and their craters (50), characterized by a *high* to *medium* quality rating (Supp. Material 1). The *low*-quality cones were defined as inferred (Fig. 2) due to the low preservation of their morphology and deposits.

Shaded relief and slope angle maps were generated using QGIS, version 3.16, based on the LiDAR DEM. These maps were used to manually outline the cone base, crater rim and crater floor by identifying and following breaks-in-slope (Fig. 3a). Then, the following morphometric parameters were either measured or calculated (Fig. 3; Tables 1 and 2 and Supp. Material 1):

(i) cone maximum (W_{max}), minimum (W_{min}) and average (W_{co}) width;
(ii) cone maximum elevation (H_{max});
(iii) cone maximum (Z_{max}), minimum (Z_{min}) and average (Z_{co}) basal elevation;
(iv) crater rim maximum height (Z_{crmax});

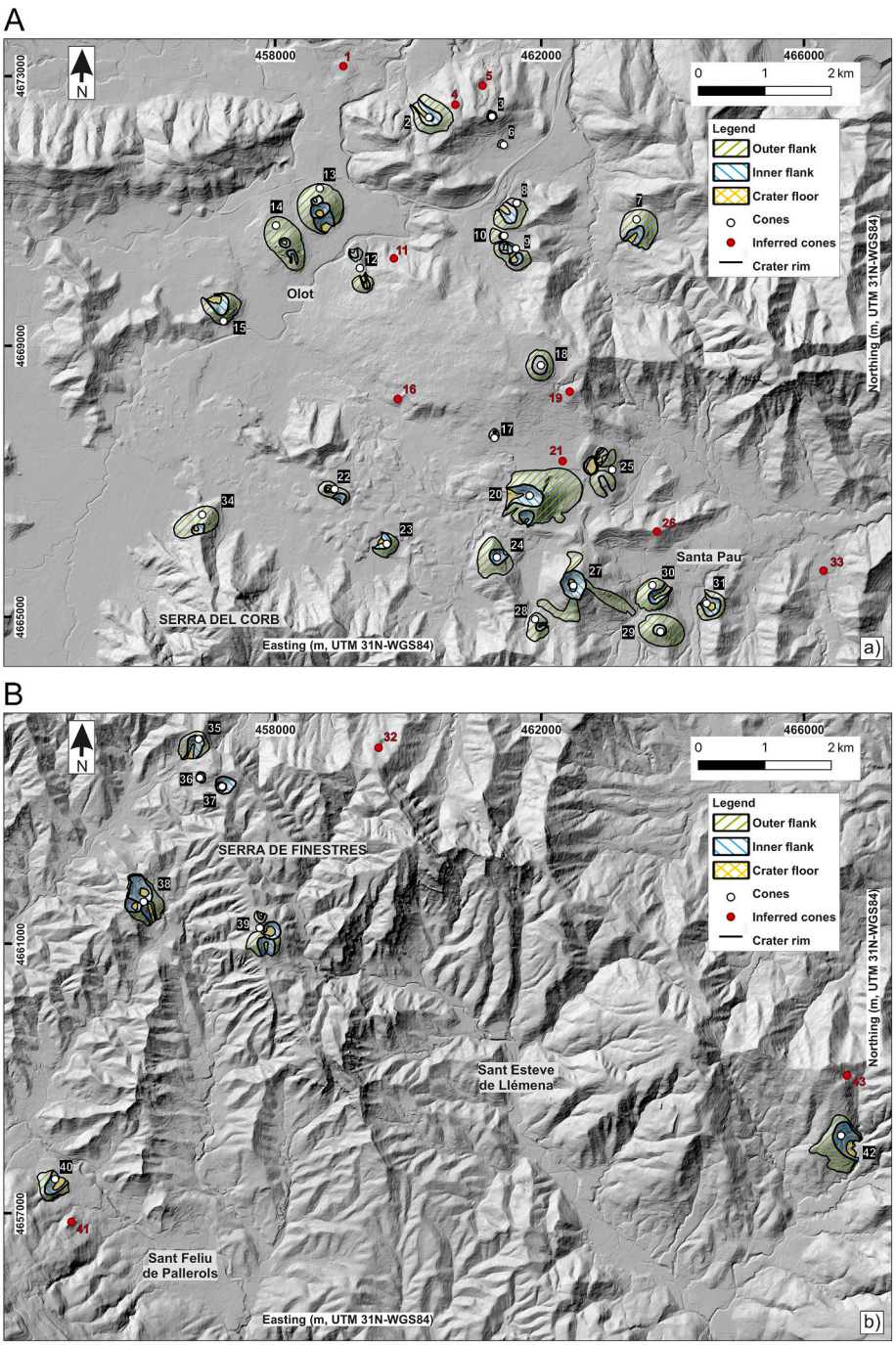

Fig. 2. Shaded relief maps derived from the 2 m DEM (Institut Cartogràfic i Geològic de Catalunya-ICGC) of the northern sector including a) Olot and Santa Pau and b) Serra de Finestres and Vall de Llémena and c) southern sector of the GVF. White dots represent monogenetic cones, red dots indicate inferred monogenetic cones (*low-quality* cones: see Supp. Material 1 for details). 1-Canya, **2-Aiguanegra (2)**, **3-Cairat (3 M)**, 4-Repassot, 5-Repás, **6-Claperols (1)**, **7-Puig de l'Ós (1)**, **8-Puig de l'Estany (1)**, **9-Puig de Bellaire (1-1)**, **10-Gengí (1)**, 11-Bac de les Tries, **12-Bisaroques (1-1) and Ca l'Isidret (2)**, **13-Garrinada (2-2-2)**, **14-Montsacopa (2)**, **15-Montolivet (1)**, 16-Can Barraca, **17-Puig Astrol (1)**, **18-Pujalós (2)**, 19-Puig de la Garsa, **20-Croscat (2)**, 21-Puig s'Agonia, **22-Cabrioler (1-1)**, **23-Puig Jordà (1)**, **24-Puig de la Costa (1)**, **25-Puig Safont (1) Puig Torn (3M) and Puig de Martinyà (1)**, 26-Puig de Mar, **27-Santa Margarida (3M)**, **28-Comadega (1)**, **29-Puig Subià (2)**, **30-Rocanegra (1)**, **31-Simon (3TR)**, 32- Pla de sa Ribera, 33-Sant Jordi, **34-Racó (3M)**, **35-Fontpobra (1)**, **36-Tuta de Colltort (3M)**, **37-Can Tià (3M)**, **38-Traiter (3M-1-1)**, **39-Puig Rodó (1), Llacunagra (3M) and Les Medes (1)**, **40-Sant Marc (2)**, 41-Puig Roig, **42-Granollers de Rocacorba (2)**, 43-Puig Montner, **44-Puig d'Àdri tuff ring and scoria cones (3TR-1-1)**, **45-Puig de la Banya del Boc (2)**, **46-Clot de l'Omera (3M)**, 47-Rocàs, **48-Crosa de Sant Dalmai maar and scoria cone (3M-1)**. In bold are the analyzed volcanoes. Numbers in parentheses represent the type of activity of each vent of the same cone. 1-magmatic, 2-magmatic-phreatomagmatic, 3-phreatomagmatic (i.e., tuff rings and maars). M-Maars, TR-Tuff Ring.

(v) crater floor minimum elevation (Z_{crmin}) and crater maximum depth (D_{crmax});

(vi) crater maximum (C_{max}), minimum (C_{min}) and average (C_{cr}) width;

(vii) craters and cones area (A) and crater perimeter (P);

C

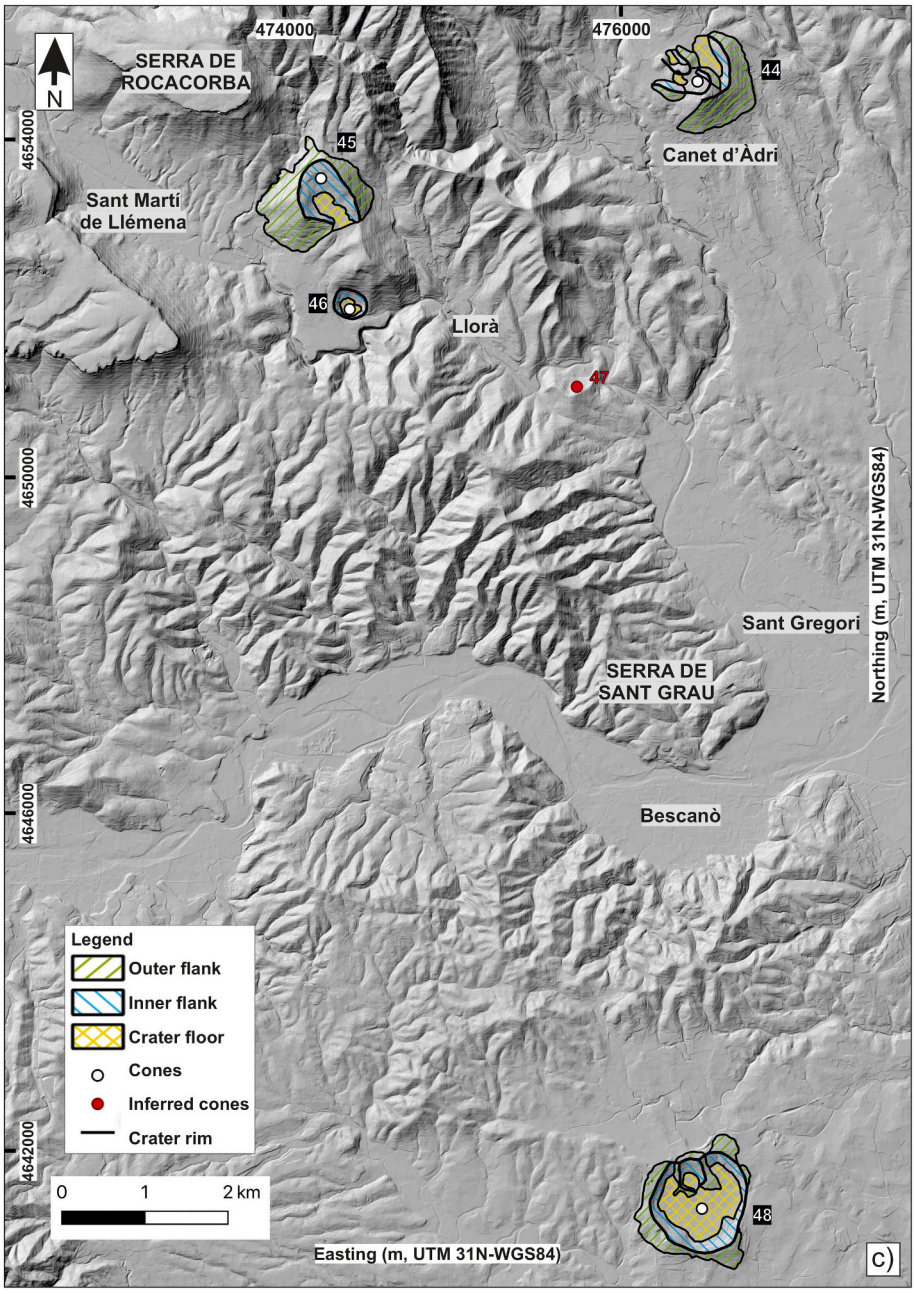

Fig. 2. (*continued*).

(vii) crater ellipticity ($C_{ellipse}$);
(viii) elongation (EL) and isoperimetric circularity (IC) of the crater;
(ix) H_{max}/W_{co}, H_{max}/W_{max}, D_{crmax}/C_{cr}, H_{max}/C_{cr}, C_{cr}/W_{co} and D_{crmax}/H_{max} ratios.

Following Aguilera et al. (2022), best-fit ellipses were estimated for the 43 best-preserved cones.

3.2. Morphological and genetic classification

Following the morphological classification proposed by Dóniz-Páez (2015), we grouped the edifices into four morphological types: *ring-shaped*, characterized by circular or slightly elliptical shape, *horseshoe-shaped* with open craters, *multiple* resulting from complex monogenetic volcanoes and coalescent edifices and *without crater* with a cone truncated shape (Fig. 4). Additionally, considering deposit characteristics (e.g., Martí et al., 2011; Martí et al., 2017; Pedrazzi et al., 2014, 2016, 2022; Planagumà et al., 2023), and following Kereszturi and Németh (2012) and Roqué et al. (2014), the volcanic cones and craters within the GVF were further classified (Fig. 5):

1. Magmatic, primarily resulting from magmatic eruption phase (e.g., Montolivet and Rocanegra; Figs. 6 and 9a and Cabrioler; Fig. 9b);
2. Magmatic-phreatomagmatic (e.g., Croscat and Garrinada; Figs. 7 and 9c and Montsacopa; Fig. 9d) with magmatic and phreatomagmatic eruption phases;
3. Phreatomagmatic tuff rings-maars, primarily characterized by phreatomagmatic eruption phases (e.g. Puig d'Àdri and La Crosa de Sant Dalmai; Fig. 8, Santa Margarida and Can Tià; Fig. 9e,f).

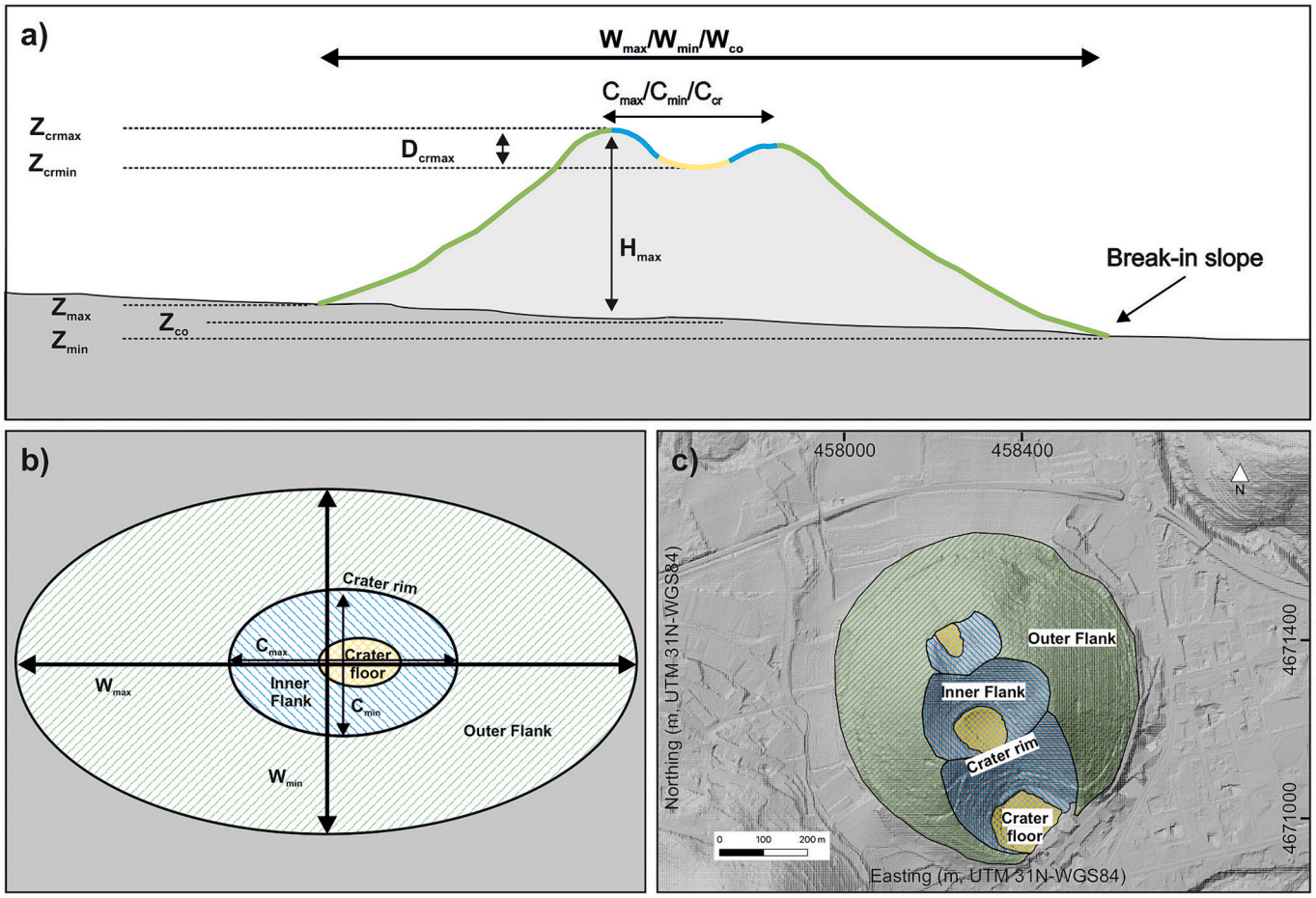

Fig. 3. a) Profile sketch of a cone showing the analyzed morphometric parameters; b) plan view sketch showing the morphometric parameters; c) example of the delimitation of the Garrinada volcano (#13; Fig. 2a). Yellow represents crater floor, blue represents the inner flanks and green the outer flanks.

Hereafter, we refer to an edifice as *magmatic* when at least 90 vol% of deposits originate from magmatic processes, *phreatomagmatic* when at least 90 % vol% of deposits are attributed to magma-water interactions and mixed (*magmatic – phreatomagmatic)* for volcanoes falling along the continuum between these two end-members.

3.3. Statistical analysis

The statistical analyses, conducted for the first time in the GVF, included bubble plots to assess potential spatial dependency of morphometric parameters (W_{co}, H_{max}, C_{cr} and D_{crmax}) (Fig. 11). Density maps for the different landforms were also generated using Gaussian kernel density estimation (KDE) (Connor et al., 2019) in QGIS, version 3.16, with a cell/pixel dimension of 0.01 and a radius defined individually for each map based on a distance matrix (Fig. 12). Following the approach suggested by Haag et al. (2019), the average vent density was calculated as the ratio of the total number of monogenetic vents (50) to the area of the convex hull, which is the polygon encompassing all dataset points. For the entire GVF, the convex hull area was approximately 315 km^2. Subsequently, a statistical analysis, using R-Studio software (https://www.rstudio.com/) (R Core Team, 2020), was performed to calculate mean (S_{mean}), median (S_{median}), maximum ($S_{maximum}$) and minimum ($S_{minimum}$) slopes as well as standard deviation ($S_{stdeviation}$), for both crater and cone flanks (Table 2 and Supp. Material 1). Additionally, density and polar diagrams of the slope values were generated for the outer flanks of cones (Supp. Material 2) and the inner flanks of craters (Supp. Material 3). Density diagrams represent the distribution of numeric variables, while polar diagrams visualize any spatial deviation of the variable.

The linear correlation among morphometric parameters (W_{co}, H_{max}, D_{crmax}, S_{mean}, C_{cr}) was examined using Pearson type correlation analysis (Fig. 13a and Supp. Material 4). This analysis provides insights into how these parameters relate to each other.

Additionally, principal component analysis (PCA) was employed, a widely utilized technique in studies of morphometry (e.g., Mazzarini et al., 2016; Uslular et al., 2021; Becerra-Ramírez et al., 2022) (Fig. 13b and Supp. Material 4). PCA linearly transforms a set of correlated morphometric parameters into a smaller number of uncorrelated variables, reducing the dimensionality of the data. We used the PCA to understand which parameters drive the variability of landform morphology in the GVF.

3.4. Eruptive sequences

The eruptive sequences depicted in Fig. 15 were identified in previous volcano stratigraphic studies conducted in the area. For instance, studies on Croscat and Santa Margarida were detailed by Martí et al. (2011), while Crosa de Sant Dalmai, Puig d'Àdri, and Puig de la Banya del Boc were investigated by Pedrazzi et al. (2014, 2016, 2022). Can Tià was studied by Martí et al. (2017) and Granollers de Rocacorba and Traiter by Planagumà et al. (2023). Recent fieldwork has included geological mapping and stratigraphy of Montolivet, Bisaroques, Rocanegra, Montsacopa, and Puig Jordà.

Table. 1
Morphometric parameters measured for the edifices of the GVF.

Parameter	Unit	Description
C_{max}	m	Crater major diameter measured on the DEMs manually, considering the largest distance between two opposite crater rim points (Wood, 1980b).
C_{min}	m	Crater minor diameter measured on the DEMs manually, considering the shortest distance between two opposite crater rim points (Wood, 1980b).
C_{cr}	m	Arithmetic mean of the crater major and minor diameters (Wood, 1980b) Ccr = (C_{max} + C_{min})/2.
Z_{crmax}	m	Crater rim maximum elevation a.s.l.
Z_{crfmin}	m	Crater floor minimum elevation a.s.l.
D_{crmax}	m	Maximum crater depth calculated as Wood (1980b) D_{crmax} = Z_{crmax}-Z_{crmin}.
W_{max}	m	Maximum cone basal diameter obtained by comparing the circumference of a manually fit ellipse Wood (1980b).
W_{min}	m	Minimum cone basal diameter obtained by comparing the circumference of a manually fit ellipse Wood (1980b).
W_{co}	m	Arithmetic mean of the cone major (W_{max}) and minor (W_{min}) diameters (Wood, 1980b) Wco = (W_{max} + W_{min})/2.
Z_{max}	m	Cone maximum basal elevation a.s.l.
Z_{min}	m	Cone minimum basal elevation a.s.l.
Z_{co}	m	Cone average basal elevation a.s.l. Zco = (Z_{max} + Z_{min})/2.
H_{max}	m	Maximum cone height calculated as Settle (1979). H_{max} = Z_{crmax}-Z_{co}.
A_{cr}	m^2	Planimetric area of the crater including crater floor and inner flanks.
A_{co}	m^2	Planimetric area of the cone including crater and outer flanks.
P_{cr}	m	Crater's perimeter.
EL	–	Elongation EL = A_{cr}/(π*(C_{max}/2)^2) where A is the area encompassed by the crater rim (Graettinger, 2018).
IC	–	Isoperimetric Circularity IC = (4*π*A_{cr})/P_{cr}^2 where A is the area encompassed by the crater rim and P is the perimeter of that same polygon (Graettinger, 2018).
$C_{ellipse}$	–	Crater ellipticity: the ratio between the minimum and maximum crater diameter (Corazzato and Tibaldi, 2006). Cellipse = (Cmin/Cmax).
S_{max}	°	Maximum slope value measured on the outer and inner flanks of each volcanic edifice. These were extracted with the R-Studio software (https://www.rstudio.com/).
S_{min}	°	Minimum slope value measured on the outer and inner flanks of each volcanic edifice. These were extracted with the R-Studio software (https://www.rstudio.com/).
S_{mean}	°	Mean slope value measured on the outer and inner flanks of each volcanic edifice. These were extracted with the R-Studio software (https://www.rstudio.com/).
S_{median}	°	Median slope value measured on the outer and inner flanks of each volcanic edifice. These were extracted with the R-Studio software (https://www.rstudio.com/).
S_{stddev}	°	Standard deviation value measured on the outer and inner flanks of each volcanic edifice. These were extracted with the R-Studio software (https://www.rstudio.com/).

4. Results

4.1. Morphometry and morpho-type

4.1.1. Genetic classification

Our analysis encompassed 43 monogenetic cones, which altogether have 50 craters (Figs. 2 and 5). Of these, 36 (84 %) are located in the northern sector of the GVF, with the remaining 7 (16 %) cones identified in the southern part. Regarding eruption characteristics, 21 (49 %) cones exhibit solely magmatic activity, while 11 (25.5 %) cones display both magmatic and phreatomagmatic phases. Additionally, 11 (25.5 %) cones are primarily associated with phreatomagmatic activity (Fig. 5).

4.1.2. Magmatic cones

The 21 magmatic cones (Fig. 5), exemplified by Montolivet and Rocanegra (Figs. 2, 6 and 9a), typically consist of weakly stratified coarse lapilli deposits rich in bombs (Fig. 6 ai, aii and bi-biii) or well-stratified to thinly laminated, medium to fine lapilli deposits, with bombs and blocks (Fig. 6 biii). Approximately 50 % of these magmatic cones show the emplacement of lava flows either at the beginning or end of the eruption (Fig. 6 aiii and Supp. Material 1).

The magmatic cones within the GVF vary significantly in size with W_{co} ranging between 144 and 758 m and H_{max} spanning between 8 and 90 m. Additionally, the craters also exhibit diversity in diameters and depths, with C_{cr} values ranging from 20 to 449 m and D_{crmax} values varying between 6 and 156 m (Table 2 and Fig. 10). The H_{max}/W_{co} ratios range from 0.04 to 0.17, C_{cr}/W_{co} ratios vary between 0.14 and 0.59 and D_{crmax}/H_{co} values span from 0.14 to 2.49. $C_{ellipse}$ show values range from 0.42 to 1 (Table 2). Furthermore, the S_{mean} values for the analyzed outer flanks range from 8° to 28° and for the inner flanks between 9° and 27° (Table 2).

4.1.3. Magmatic-phreatomagmatic cones

The volcanic deposits of these landforms (11 in total), characterized by both magmatic and phreatomagmatic phases (e.g., Croscat and La Garrinada; Figs. 2, 7 and 9c), consist of thin to thick beds formed of well-vesiculated lapilli with occasional bombs (Fig. 7 ai-aii and bi-bii). Additionally, they exhibit subordinate thin to medium beds of lithic-rich, sometimes laminated, poorly-vesiculated lapilli layers (Fig. 7 aiii and biii). These landforms have W_{co} values ranging between 238 and 1593 m and H_{max} values between 19 and 185 m. Furthermore, C_{cr} and D_{crmax} fall between 122 and 734 m and between 12 and 184 m, respectively (Table 2 and Fig. 10). The H_{max}/W_{co} ratios are between 0.08 and 0.15, C_{cr}/W_{co} ratios range between 0.18 and 0.53 and D_{crmax}/H_{max} ratios range from 0.11 to 2.62. $C_{ellipse}$ values range from 0.45 to 0.85 (Table 2). Moreover, the S_{mean} for the analyzed outer flanks is between 17° and 25° and for the inner flanks between 13° and 30° (Table 2).

4.1.4. Phreatomagmatic tuff rings-maars

11 phreatomagmatic volcanoes (Fig. 5) include 2 tuff rings and 9 maars, such as Puig d'Àdri, La Crosa de Santa Dalmai and Can Tià (Figs. 2, 8 and 9f). These landforms are often associated with low-lying sedimentary areas as observed with Puig d'Àdri (Figs. 2 and 8a), while maars typically form along Palaeozoic basement blocks as seen in La Crosa de Sant Dalmai (Figs. 2 and 8b).

The volcanic deposits primarily consist of medium-thick beds of lithic-rich explosion breccia beds with impact bomb sags (Fig. 8 bi) along with poorly sorted, massive (Fig. 8 aii) and parallel and cross laminated (Fig. 8 ai and biii) lithic-rich thin lapilli layers and subordinate Strombolian deposits (Fig. 8 aiii and bii). These phreatomagmatic landforms exhibit W_{co} values ranging from 190 to 1755 m and H_{max} values between 15 and 151 m. Additionally, C_{cr} and D_{crmax} values fall within the range of 143 to 1150 m and 13 to 94 m, respectively (Table 2 and Fig. 10). The H_{max}/W_{co} ratios range between 0.03 and 0.13, C_{cr}/W_{co} ratios span from 0.27 to 0.83 and D_{crmax}/H_{max} values range from 0.44 to 2. $C_{ellipse}$ values are situated between 0.66 and 0.99 (Table 2). Furthermore, the S_{mean} for the analyzed outer flanks ranges from 9° to 26° and for the inner flanks between 11° and 39° (Table 2).

4.1.5. Comparing landforms

Our study highlights that approximately 32 cones (85 %) have H_{max} values <100 m, with 6 (16 %) having values between 101 and 220. Regarding A_{co} values, 22 (61 %) have areas <0.2 km^2, 9 (25 %) between 0.2 and 0.5 km^2 and 5 (14 %) >0.5 km^2.

In the GVF, magmatic and magmatic-phreatomagmatic cones exhibit some overlap in terms of H_{max}/W_{co}, C_{cr}/W_{co} and D_{crmax}/H_{co} ratios (Table 2). Tuff rings-maars generally show slightly lower H_{max}/W_{co} ratios (Table 2).

When examining the morphometric parameters, there is a noticeable overlap among various volcanoes with different eruption histories (Fig. 10). However, slight differences are noted for W_{co} (Fig. 10b,e) and H_{max} (Fig. 10b,d) between magmatic and magmatic-phreatomagmatic cones (Table 2).

In the context of monogenetic volcanoes in the GVF, they generally align with the global trend observed in Fig. 10a when examining the

Table. 2
Values of morphometric parameters of the GVF edifices.

Morphometric parameters	Magmatic cones			Magmatic-phreatomagmatic cones			Phreatomagmatic tepra rings-maars		
	Maximum	Minimum	Average	Maximum	Minimum	Average	Maximum	Minimum	Average
W_{max} (m)	865	151	532	1.606	252	879	1.755	190	791
W_{min} (m)	689	136	454	1.581	223	697	1.754	183	706
W_{co} (m)	758	144	493	1.593	238	789	1.754	187	748
H_{max} (m)	90	8	46	185	19	93	151	15	77
S_{mean} (°)	28	8	20	25	17	21	26	9	18
C_{max} (m)	563	22	240	850	132	356	1.2	148	417
C_{min} (m)	335	17	169	618	113	243	1.1	137	343
C_{cr} (m)	449	20	204	734	122	299	1.15	143	380
D_{crmax} (m)	156	6	57	184	12	96	94	13	65
S_{crmean} (°)	27	9	18	30	13	22	39	11	19
$C_{ellipse}$ (Crater Ratio)	1	0,42	0,73	0,85	0,45	0,71	0,99	0,66	0,85
Elongation (EL)	1,22	0,34	0,76	0,86	0,24	0,7	1,08	0,3	0,81
Isoperimetric Circularity (IC)	0,97	0,31	0,78	0,97	0,57	0,81	1,04	0,44	0,88
H_{max}/W_{co}	0,17	0,04	0,09	0,15	0,08	0,12	0,14	0,03	0,08
H_{max}/W_{max}	0,16	0,02	0,08	0,14	0,07	0,1	0,13	0,03	0,08
D_{crmax}/C_{cr}	0,56	0,07	0,26	0,53	0,04	0,32	0,59	0,05	0,23
H_{max}/C_{cr}	0,64	0,07	0,27	0,8	0,16	0,36	0,44	0,04	0,2
C_{cr}/W_{co}	0,59	0,14	0,38	0,53	0,18	0,38	0,83	0,27	0,6
D_{crmax}/H_{max}	2,49	0,14	1,13	2,62	0,11	1,22	2	0,44	1,21
Deposit features	Poorly or well-stratified to thinly laminated fine to coarse vesiculated lapilli deposits with loose bombs and blocks Massive lava flows			Thick well-vesiculated lapilli and bomb beds with subordinate thin to medium beds of lithic-rich, sometimes laminated, poorly-vesiculated lapilli layers Massive lava flows			Medium-thick beds of lithic-rich explosion breccia beds with bomb sags along with poorly sorted, massive and parallel and cross laminated lithic-rich thin lapilli layers		
Interpretation	Fallout, ballistic blocks and bombs and lava flows			Fallout, ballistic blocks and bombs and dilute PDCs and lava flows.			Fallout, ballistic blocks and bombs and dense and dilute PDCs.		
Eruption styles	Magmatic eruption			Magmatic eruption and magma-water interaction with aquifers			Mainly magma-water interaction with aquifers		
Principal distinguishing morphometric characteristics	Horseshoe and ring-shaped			Horseshoe-shaped and multiple			Ring and horseshoe-shaped		

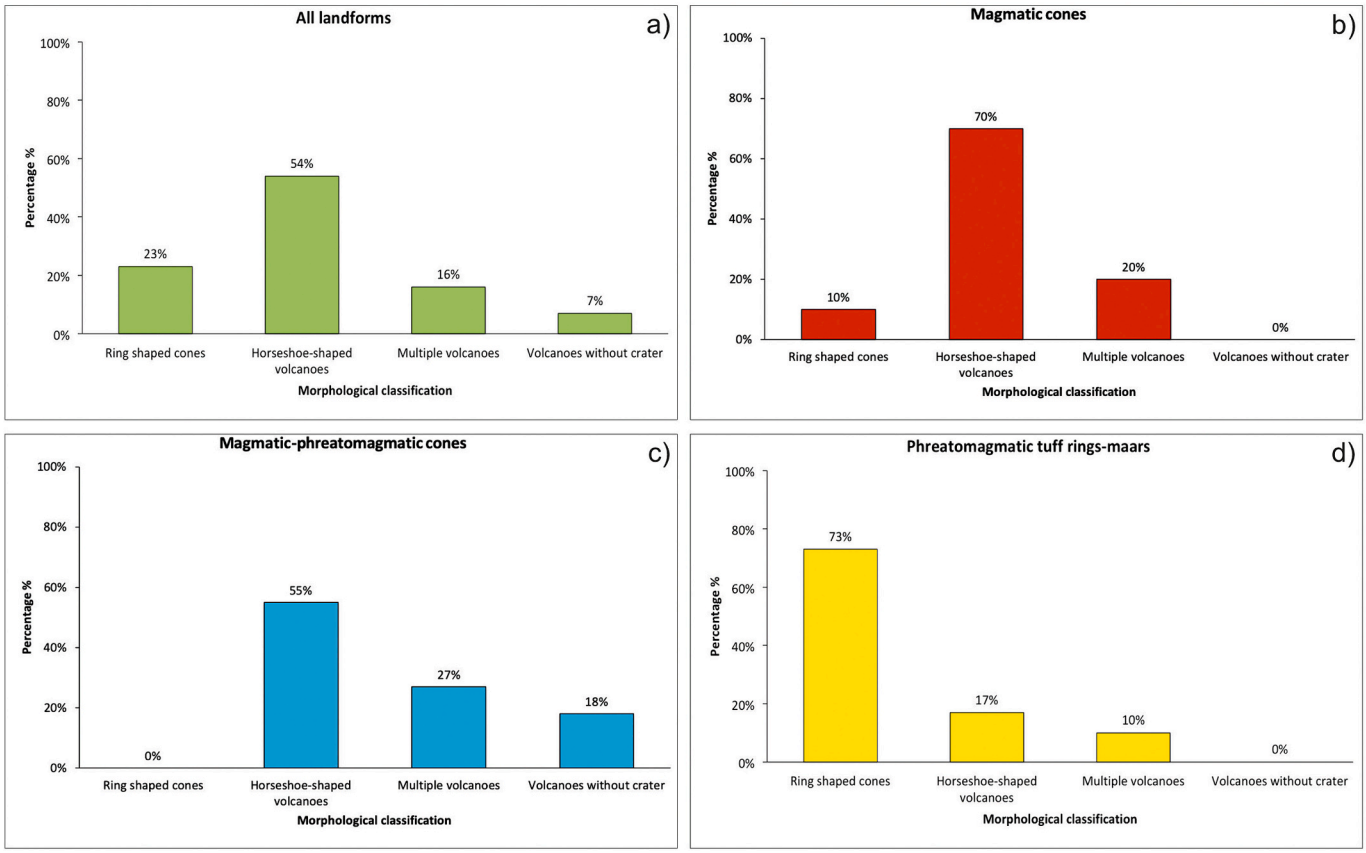

Fig. 4. Morphological classification of monogenetic volcanoes of the GVF edifices grouped into four morphological types: *ring-shaped*, *horseshoe-shaped*, *multiples* and *without crater* (Dóniz-Páez, 2015): a) all landforms; b) magmatic cones; c) magmatic-phreatomagmatic cones; d) phreatomagmatic tuff rings and maars.

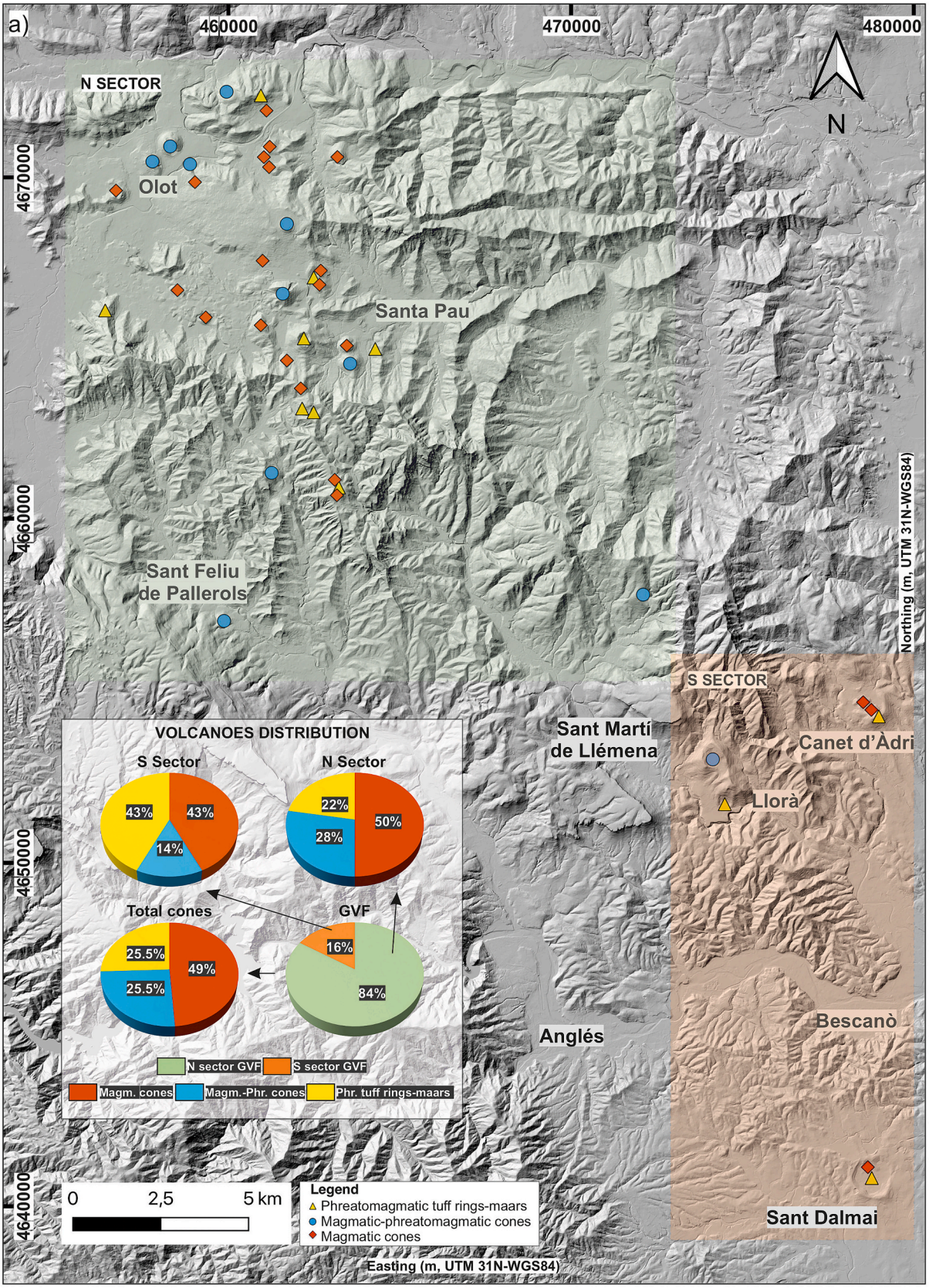

Fig. 5. Shaded relief map of the 2 m DEM (Institut Cartogràfic i Geològic de Catalunya-ICGC) of the northern (light green) and southern (light orange) GVF areas. Cones are represented as follows: magmatic (red diamonds), magmatic-phreatomagmatic (blue circles) and phreatomagmatic tuff rings-maars (yellow triangles). Pie charts depict their distribution.

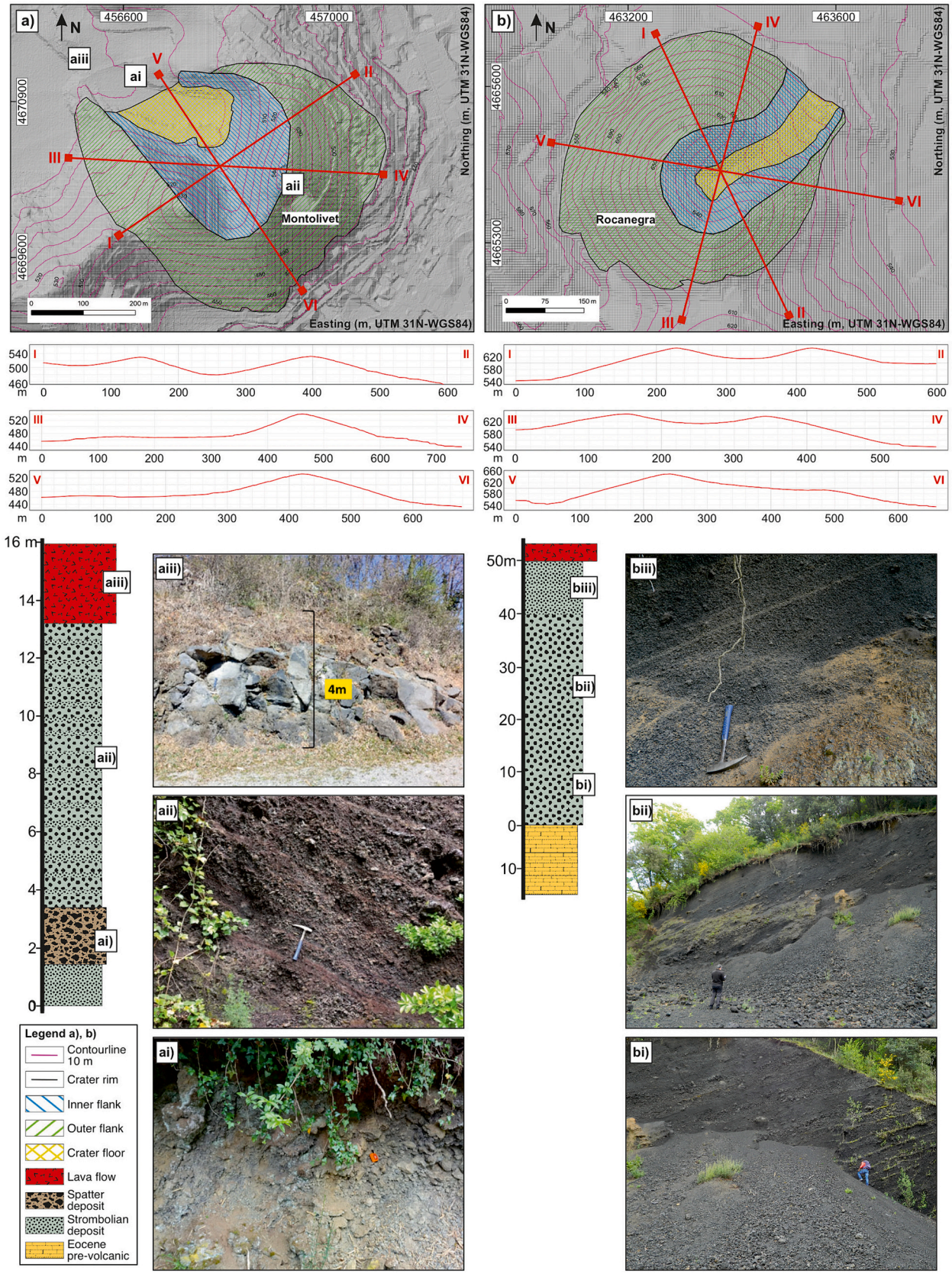

Fig. 6. Examples of magmatic cones in the GVF. DEM-derived shaded relief image with contour lines and topographic profiles of: a) Montolivet volcano with ai) spatter deposits; aii) scoria and lapilli bombs beds and aiii) lava flow; b) Rocanegra volcano with bi) scoria and lapilli bombs beds; bii) bombs beds and biii) stratified lapilli deposits.

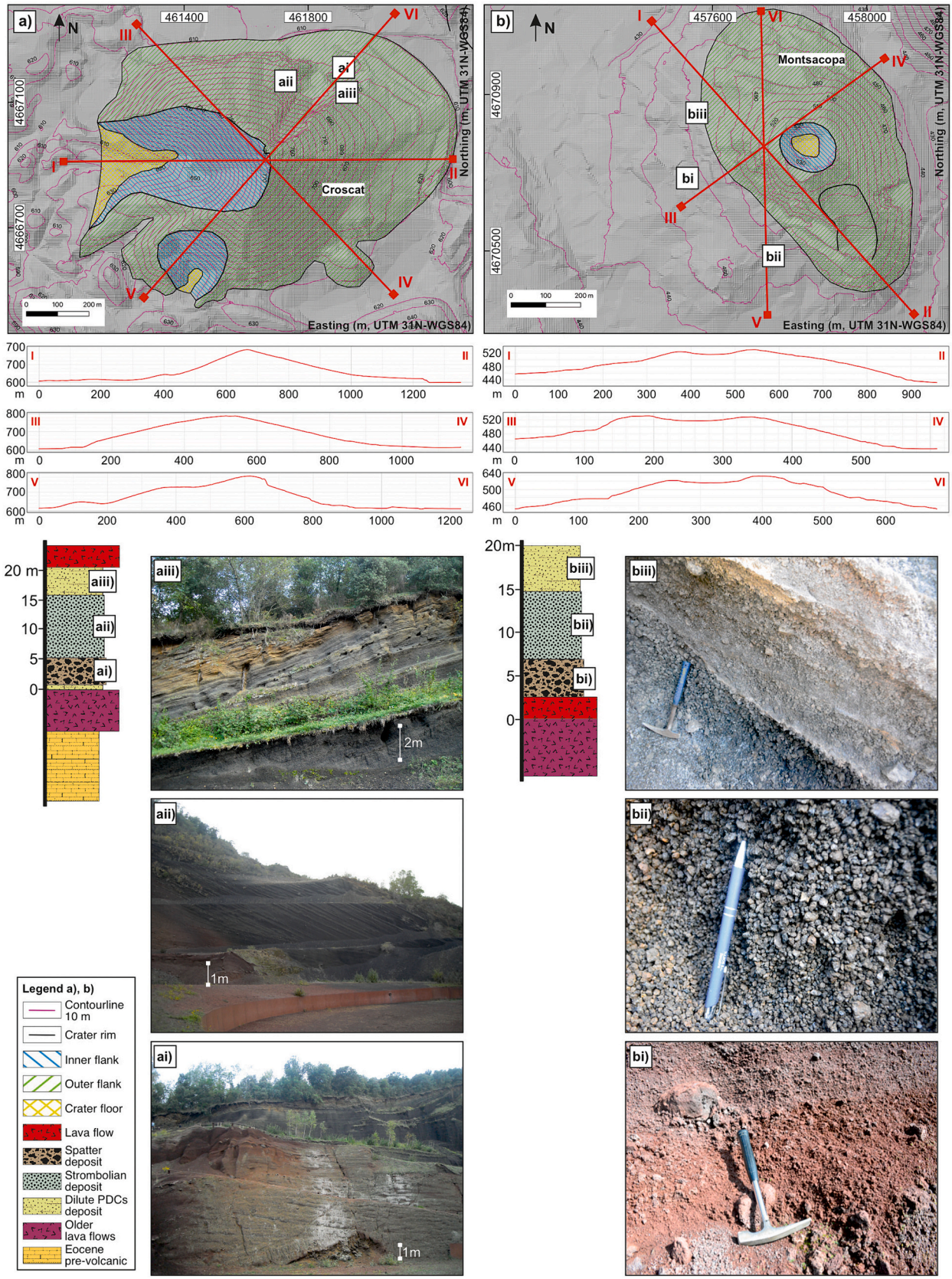

Fig. 7. Examples of cones with magmatic and phreatomagmatic phases in the GVF. DEM-derived shaded relief image with contour lines and topographic profiles of: a) Croscat volcano with ai) spatter and scoria and lapilli deposits; aii) stratified lapilli deposits and aiii) lithic-rich laminated deposits in the upper part of the sequence; b) Montsacopa volcano with bi) spatter deposits; bii) massive clast-supported lapilli deposits and biii) lithic-rich laminated and massive deposits with poor vesiculated scoriae.

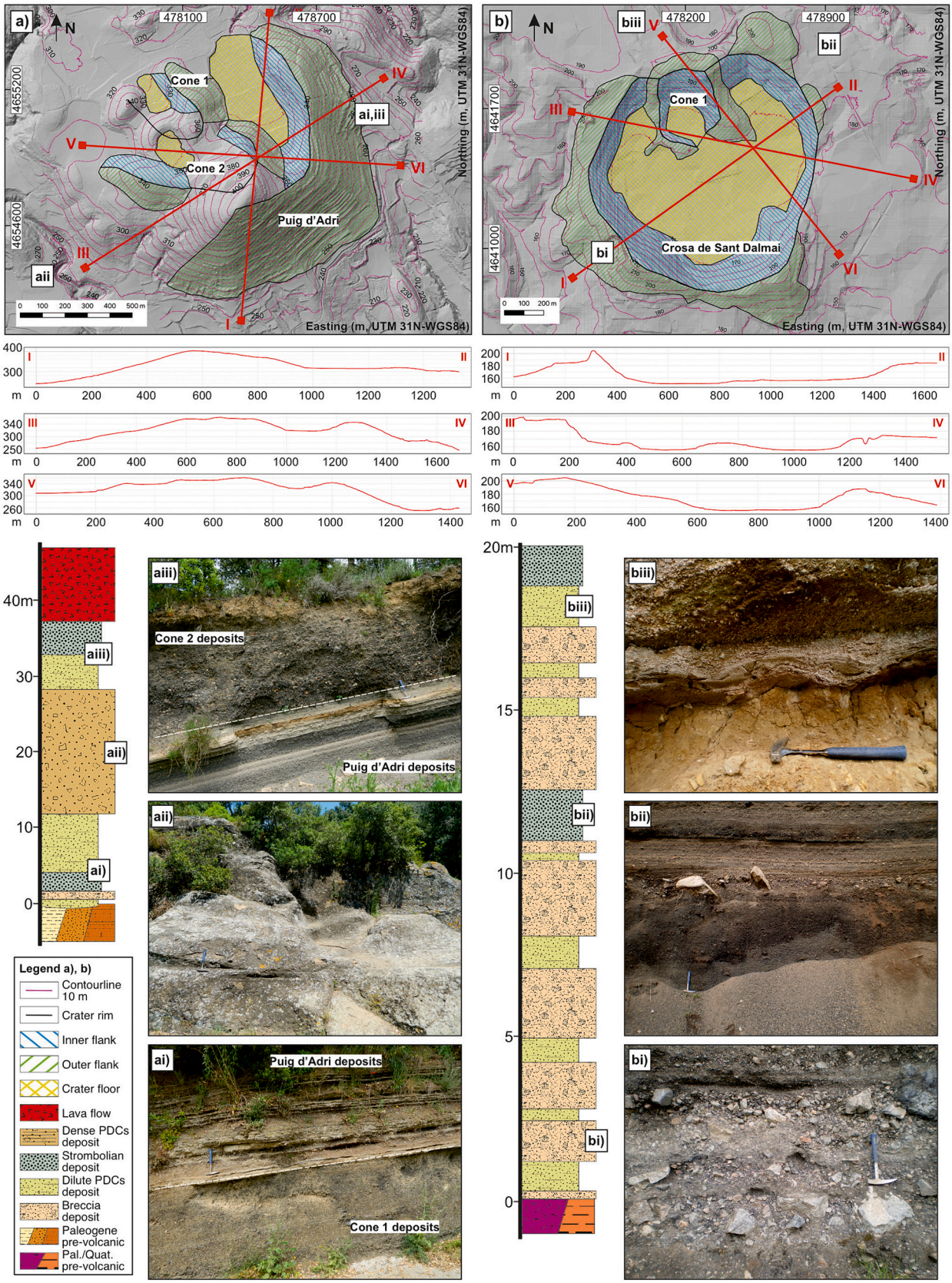

Fig. 8. Examples of cones with mainly phreatomagmatic deposits in the GVF. DEM-derived shaded relief image with contour lines and topographic profiles of: a) Puig d'Àdri volcano with ai) Strombolian and stratified lithic-rich deposits; aii) massive slightly stratified deposits and aiii) stratified lithic-rich laminated and Strombolian deposits; b) La Crosa de Sant Dalmai volcano with bi) breccia deposits; bii) Strombolian and breccia deposits and biii) laminated deposits with cross stratification.

Fig. 9. Several examples of different types of edifices and morphologies in the GVF (a-f) and their location (g): horseshoe-shaped volcanoes: a) Montolivet (1), b) Cabrioler (1), ring-shaped landforms: e) Santa Margarida (3 M) f) Can Tià (3 M); multiple volcanoes: c) Garrinada (2) and d) Montsacopa (2). 1-Magmatic, 2-magmatic-phreatomagmatic, 3-Phreatomagmatic tuff rings-maars. M-Maars. *Credit:* Eduard Masdeu.

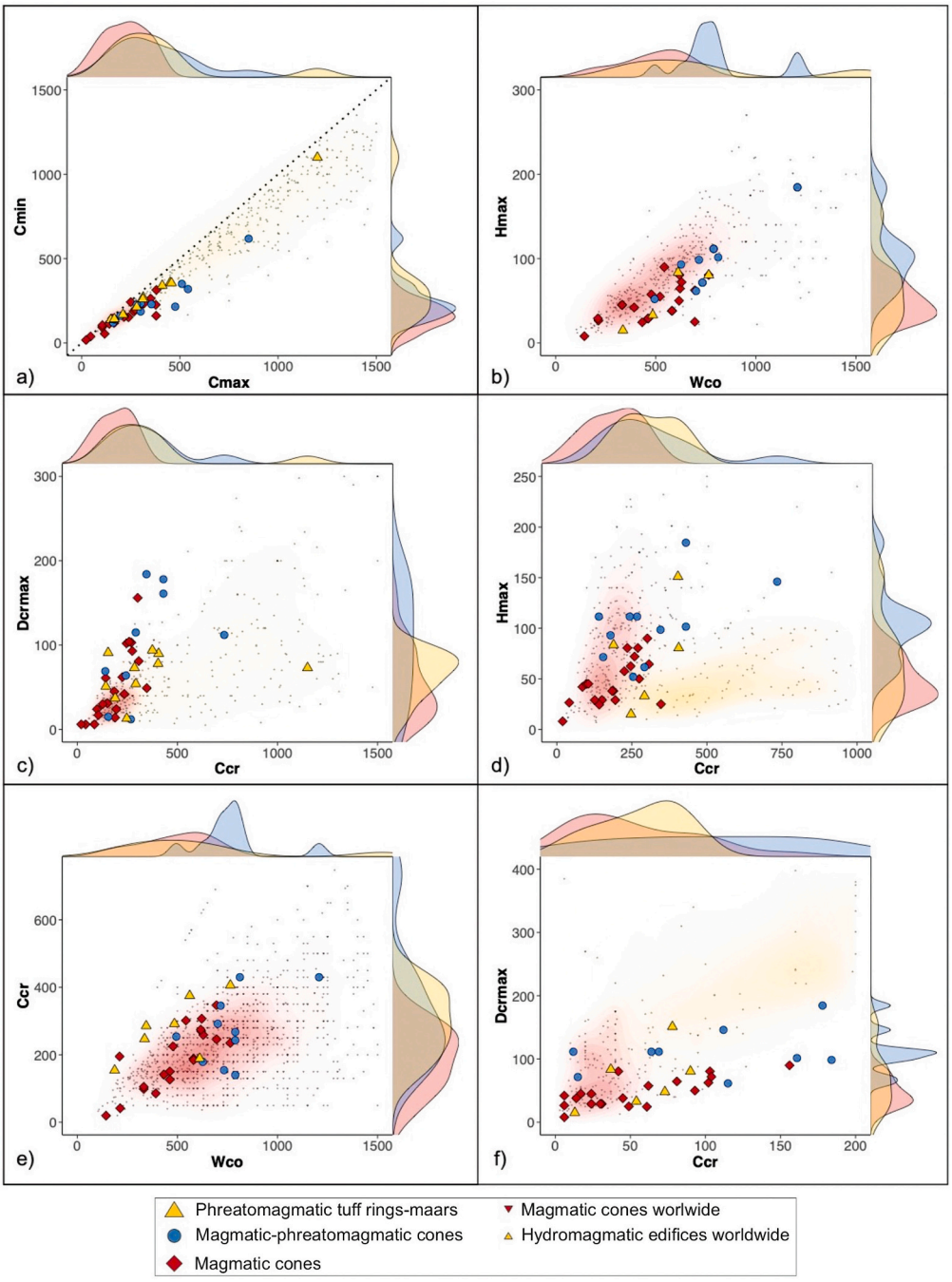

Fig. 10. Morphometric relations for the best preserved GVF craters and cones: a) maximum (C_{max}) vs. minimum (C_{min}) crater diameters; b) mean cone diameter (W_{co}) vs. maximum cone height (H_{max}); c) mean crater diameter (C_{cr}) vs. maximum crater depth (D_{crmax}); d) mean crater diameter (C_{cr}) vs. maximum cone height (H_{max}); e) mean cone diameter (W_{co}) vs. mean crater diameter (C_{cr}); f) maximum crater depth (D_{crmax}) vs. maximum cone height (H_{max}). For comparison yellow and red shaded areas correspond to magmatic and phreatomagmatic edifices worldwide (Gabor Kereszturi, unpublished data). Panels on the top and right side display kernel density estimates of the morphometric parameters represented in the x- and y-axis, respectively.

parameters C_{max} vs C_{min}. However, they appear to deviate below the global trend for W_{co} vs H_{max} (Fig. 10b), indicating a flatter morphology as well as for the fields of C_{cr} vs D_{crmax} (Fig. 10c) and C_{cr} vs H_{max} (Fig. 10d) where more scattered values are evident.

Based on their geometry (Supp. Material 1), the EL were categorized into two groups: 42 circular (EL $<$ 1.2) and 1 slightly elongated (EL between 1.2 and 1.4). This indicates that the majority of monogenetic craters within the GVF are not elongated.

4.1.6. Geomorphology and morpho-type

Following the morphological classification proposed by Dóniz-Páez (2015), 23 horseshoe-shaped volcanoes represent 54 % of the whole population. They are followed by 10 ring-shaped landforms, which account for 23 % of the population. 7 multiple volcanoes constitute 16 % of the population, while 3 volcanoes without craters make up 7 % of the total (Fig. 4a).

In terms of each type of volcanic landform, magmatic cones consist of 15 (70 %) horseshoe-shaped volcanoes, 2 (10 %) ring-shaped landforms, and 4 (20 %) multiple volcanoes (Fig. 4b). Magmatic-phreatomagmatic cones are characterized by 6 (55 %) horseshoe-shaped volcanoes, 3 (27 %) multiple volcanoes, and 2 (18 %) volcanoes without craters (Fig. 4c). Tuff rings-maars predominantly feature 8 (73 %) ring-shaped cones, 2

(17 %) horseshoe-shaped volcanoes, and 1 (10 %) multiple volcano (Fig. 4d).

4.2. Spatial orientation and distribution

The largest values of W_{co} (up to 1755 m; Table 2 and Fig. 11a) and C_{cr} (up to 11,150 m; Table 2 and Fig. 11c) are predominantly found in the southern sector, encompassing the Vall de Llémena area and La Selva depression (Figs. 1c and 2). They correspond to tuff rings and maars such as Puig d'Àdri and La Crosa de Sant Dalmai (Fig. 2). In contrast, the highest concentration of volcanic cones with the greatest H_{max} (up to 185 m; Table 2 and Fig. 11b) and D_{crmax} (up to 184 m; Table 2 and Fig. 11d) values are located in the Olot and Santa Pau areas, in the northern sector of the GVF (Fig. 1c), including examples as Croscat (Fig. 2).

The GVF exhibits an average vent density of 1.6×10^{-1} vents/km^2, with the highest vent density in the northern region (Fig. 12a), particularly around Olot and Santa Pau areas (Figs. 1c and 2).

KDE reveals distinct distributions for different types of vents: magmatic and magmatic-phreatomagmatic vents are primarily distributed in the northern Olot and Santa Pau areas (Fig. 12b,c). In contrast tuff rings-maars show a more dispersed distribution (Fig. 12d).

4.3. Correlation between morphometric parameters

The results from the correlation matrix and Pearson's correlation coefficient highlight a significant correlation between C_{cr} and W_{co}, regardless of the type of volcanic landform (Fig. 13a). Particularly in magmatic cones, there's a strong correlation observed between D_{crmax} and H_{max} as well as between W_{co} and H_{max}.

Similar strong correlations between these parameters are also evident in magmatic-phreatomagmatic landforms, albeit with fewer representative edifices. Additionally, slope angles (represented as S_{mean}) and C_{cr} moderately correlate with H_{max} in magmatic cones.

PCA results indicate that PC1 and PC2 account for approximately 83 % of the variance (Fig. 13b and Supp. Material 4). Variations in PC1 variations primarily reflect changes in parameters such as W_{co}, H_{max}, D_{crmax}, C_{cr} and D_{crmax}, while PC2 variance is predominantly governed by S_{mean}. The PCA reinforces the robust correlations observed between D_{crmax} and H_{max} as well as between W_{co} and C_{cr}.

4.4. Relative ages

Morphometry-based geochronology in monogenetic fields often relies on parameters such as S_{mean} and the H_{co}/W_{co} ratio (Colton, 1937; Breed, 1964; Wood, 1980a, 1980b; Dohrenwend et al., 1986). In the GVF, however, no discernible pattern in these parameters is evident when considering the type of edifice (Fig. 14a). Similarly, the relationship between S_{mean} and the absolute ages of volcanic landforms (Fig. 14b) does not reveal a clear trend, as also observed if compared to global datasets (Kereszturi, unpublished data), and only a broadly decreasing trend of S_{mean} with time is observed (Fig. 14b). No clear patterns are observed considering the ratios H_{max}/W_{co} and D_{crmax}/C_{cr} vs. ages (Fig. 14c).

Ages were determined using various dating techniques, including C-14 analysis (Burjachs, 1985; Pedrazzi et al., 2014), thermoluminescence in plagioclases (Guérin and Valladas, 1980; Guérin et al., 1985) and sediments, isotopic dating using K/Ar (Donville, 1973; Guérin et al., 1985), U-Th (Pedrazzi et al., 2014), Ar/Ar (Lewis et al., 2000), stratigraphy (Mallarach and Riera, 1981, Mallarach, 1982, Mallarach i Carrera, 1998) and biostratigraphy (Bolós, 1925) (see: Supp. Material 1). Furthermore, for volcanoes lacking absolute ages, they have been positioned along the timeline with relative ages from the Pleistocene (Bolós et al., 2014a, b).

4.5. Type of eruptive activity

Among the total eruptions analyzed, 16 (46 %) began with an initial phreatomagmatic activity. Specifically, 4 (12 %) of the total eruptions consisted solely of a single phreatomagmatic phase (e.g., Santa Margarida; Fig. 15), while 12 (34 %) exhibited more complex eruptive sequences. These include combinations of phreatomagmatic and magmatic explosive phases (e.g., Aiguanegra; Fig. 15), or such sequences followed by an effusive episode (e.g., Puig de la Banya del Boc; Fig. 15), and more intricate behaviors as observed in Can Tià, Granollers, or Puig d'Àdri (Fig. 15).

19 (54 %) eruptions show an initial phase predominantly magmatic explosive. 7 (20 %) of the total were exclusively associated with magmatic explosive stages (e.g., Puig de la Costa; Fig. 15), while others involved combinations of magmatic explosive and effusive phases, as seen in Rocanegra (Fig. 15). Some eruptions also featured a final phreatomagmatic phase in addition to earlier magmatic activity, exemplified by Montsacopa (Fig. 15). Moreover, 5 (14 %) of the eruptive sequences demonstrated even more complex combinations, as observed in La Garrinada, Les Medes, and Croscat (Fig. 15).

5. Discussion

5.1. Imprinting eruptive styles on the morphology

The monogenetic landforms of the GVF are characterized by approximately 50 % of scoria cones (Fig. 5), primarily formed through magmatic eruption styles, due to predominantly Strombolian eruptions (Németh and Kereszturi, 2015). The remaining 50 % are evenly distributed between magmatic-phreatomagmatic volcanoes and phreatomagmatic tuff rings-maars (Fig. 5) where magma/water interactions have partially or totally drove the fragmentation process (e.g., Wohletz, 1986; Büttner and Zimanowski, 1998).

Scoria cones within the GVF show deviation from the 'ideal' scoria cone described by Porter (1972), Wood (1980a, b) and Fornaciai et al. (2012) in terms of morphometric parameters such as H_{max}/W_{max}, C_{cr}/W_{co} and S_{mean} (Table 2). The shape of volcanic landforms shows a close relation with the pre-eruptive topography (Dóniz-Páez, 2001; Dóniz et al., 2011). Volcanoes tend to be ring-shaped or horseshoe-shaped with circular to sub-circular elongations when the pre-eruptive surface inclination is $<10^{\circ}$. In contrast, slopes $>10^{\circ}$ favor the formation of open craters and volcanoes with elongated plans (Dóniz et al., 2011). Within the GVF, two primary morphological types dominate: horseshoe-shaped cones, accounting for 54 %, and ring-shaped cones comprising 23 % of the total (Fig. 4a).

Approximately 80 % of magmatic cones in the GVF exhibit ring and horseshoe-shaped morphologies (Fig. 4b), with 83 % of them emplaced on flat terrain. The horseshoe-shaped morphology of these cones mainly results from effusive activity, often associated with crater and/or flank breaching induced by lava effusion (Martí, 2000). Examples include volcanoes like Puig Jordà, Rocanegra, Montolivet, Puig de l'Estany, Fontpobra, and Claperols (Figs. 2 and 15), where lava flows during the final stages of eruption are common.

Furthermore, spatter accumulation, agglutination, and welding can significantly influence the morphology of scoria cones by increasing slope angles (e.g., Bemis and Ferencz, 2017). This phenomenon is observed at volcanoes such as Montolivet and Bisaroques (Fig. 2) where spatter and welding were responsible for maintain and stabilize the flank morphology and overall geometry of the edifice. Variations in average grain size, degree of sorting, angularity, and density also play crucial roles in shaping magmatic cones, affecting sediment angle of repose (Bemis and Ferencz, 2017). Magmatic cones in the GVF typically exhibit varying grain sizes ranging from lapilli to blocks and bombs (e.g., Montolivet and Rocanegra; Fig. 6; cf. Riedel et al., 2003). Moreover, irregularly shaped cones can result from processes such as the eruption of multiple vents or vent migration along fissures (e.g., Tibaldi, 1995;

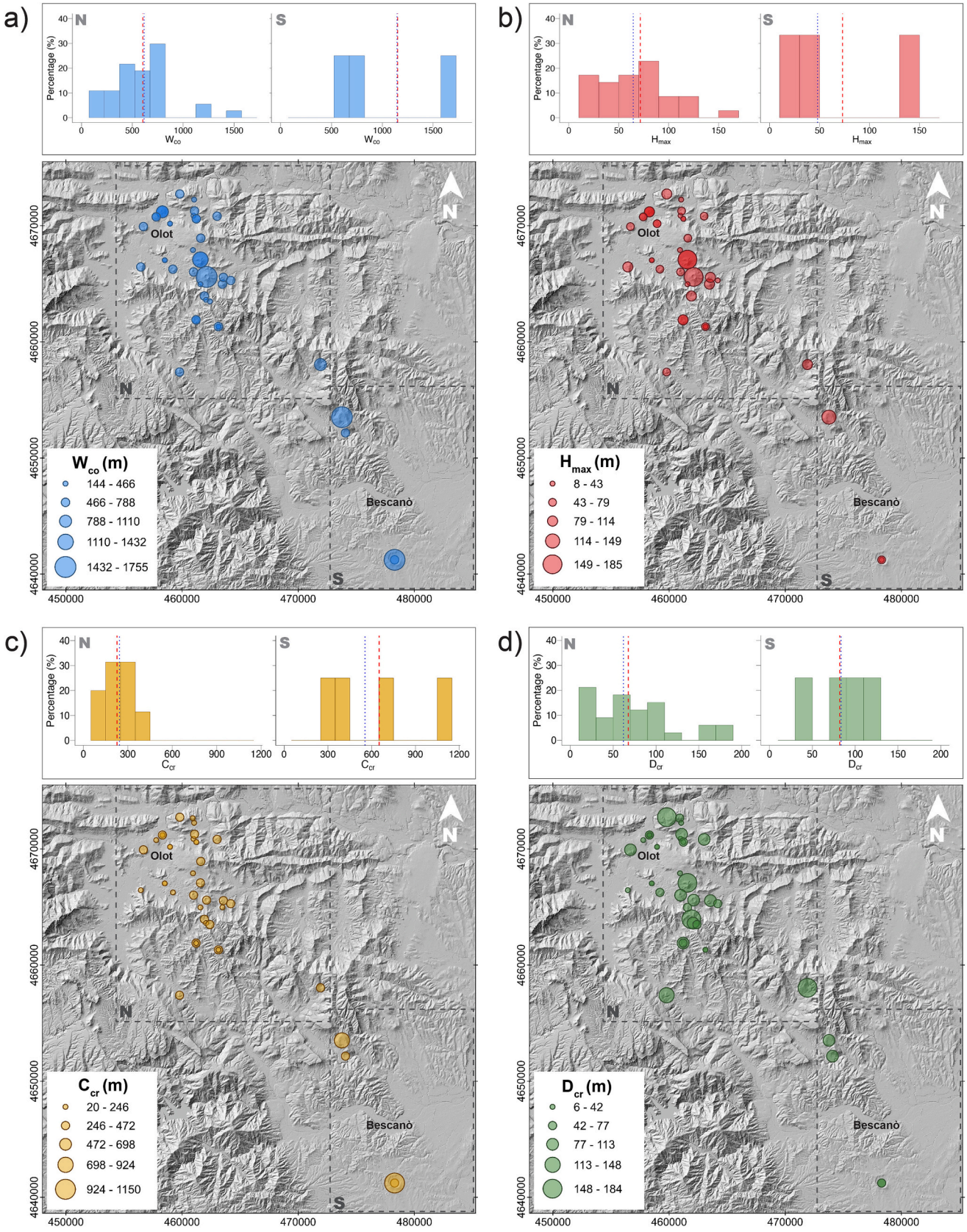

Fig. 11. Bubble plots showing the spatial pattern of key morphometric parameters combined with two density histograms, one per GVF sector. a) mean cone diameter-W_{co}; b) maximum cone height-H_{max}; c) mean crater diameter-C_{cr}; d) maximum crater depth- D_{crmax}. Blue dotted and red squared lines represent respectively the median and mean values.

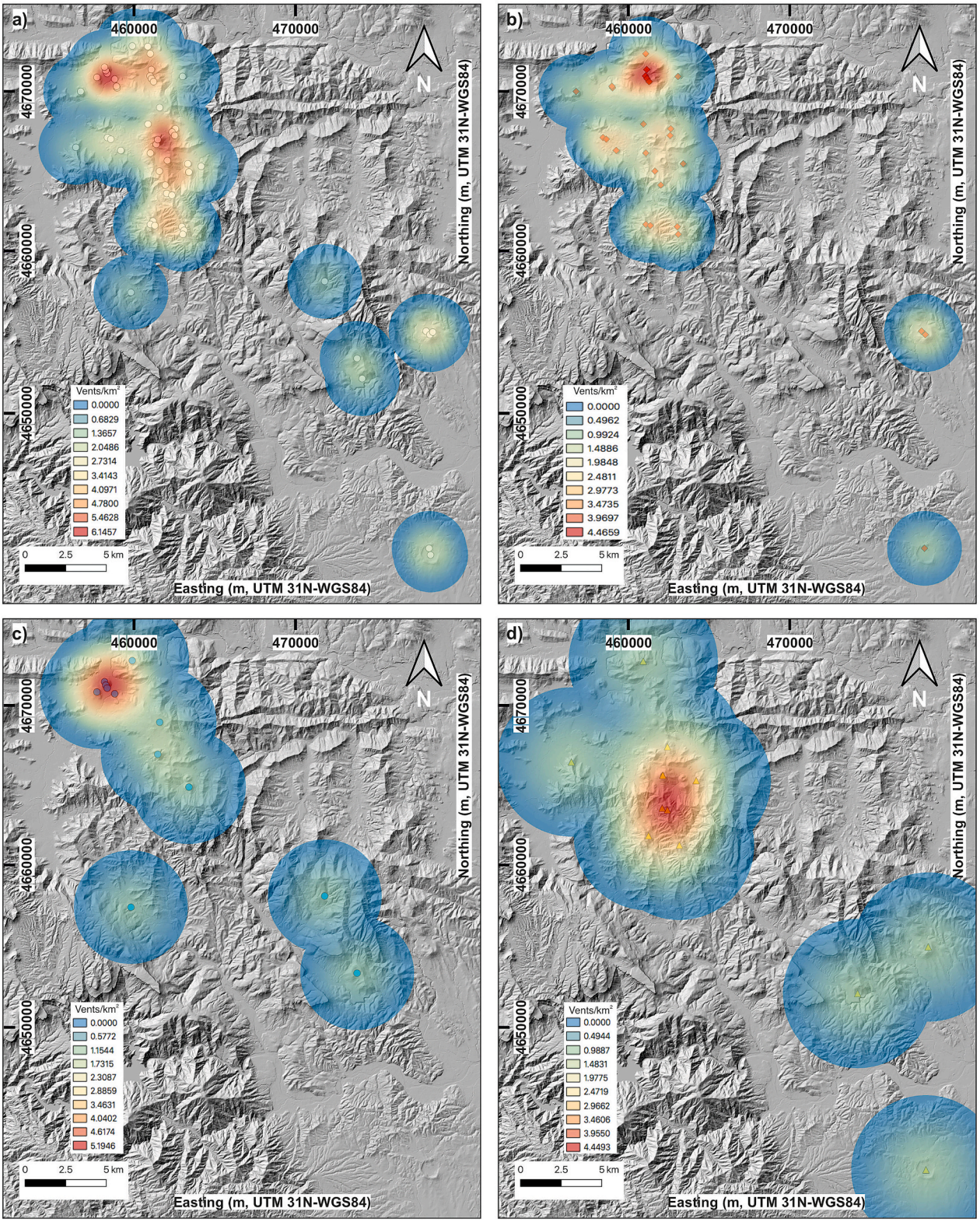

Fig. 12. KDE for monogenetic volcanoes: a) all GVF volcanic vents; b) magmatic vents; c) magmatic-phreatomagmatic vents; d) phreatomagmatic tuff rings-maars.

Corazzato and Tibaldi, 2006) as documented at Bisaroques, Puig de Bellaire and Cabrioler volcanoes (Fig. 2). Given the available absolute ages and stratigraphy-based age constraints, the observed morphometric variations are rather interpreted to be due to eruptive processes and vent conditions, including pre-eruptive terrain inclination, eruptive history, grain-size and welding/agglutination differences. These variations are reflected in the correlations observed in Pearson's correlation and PCA analyses (Fig. 13), indicating significant relationships between parameters like D_{crmax} and H_{max}, as well as W_{co} and C_{cr}, often linked to fragmentation intensity (Grosse et al., 2020).

Magmatic-phreatomagmatic cones are predominantly horseshoe-shaped (55 %) and multiple (27 %) (Fig. 4c), while tuff rings-maars

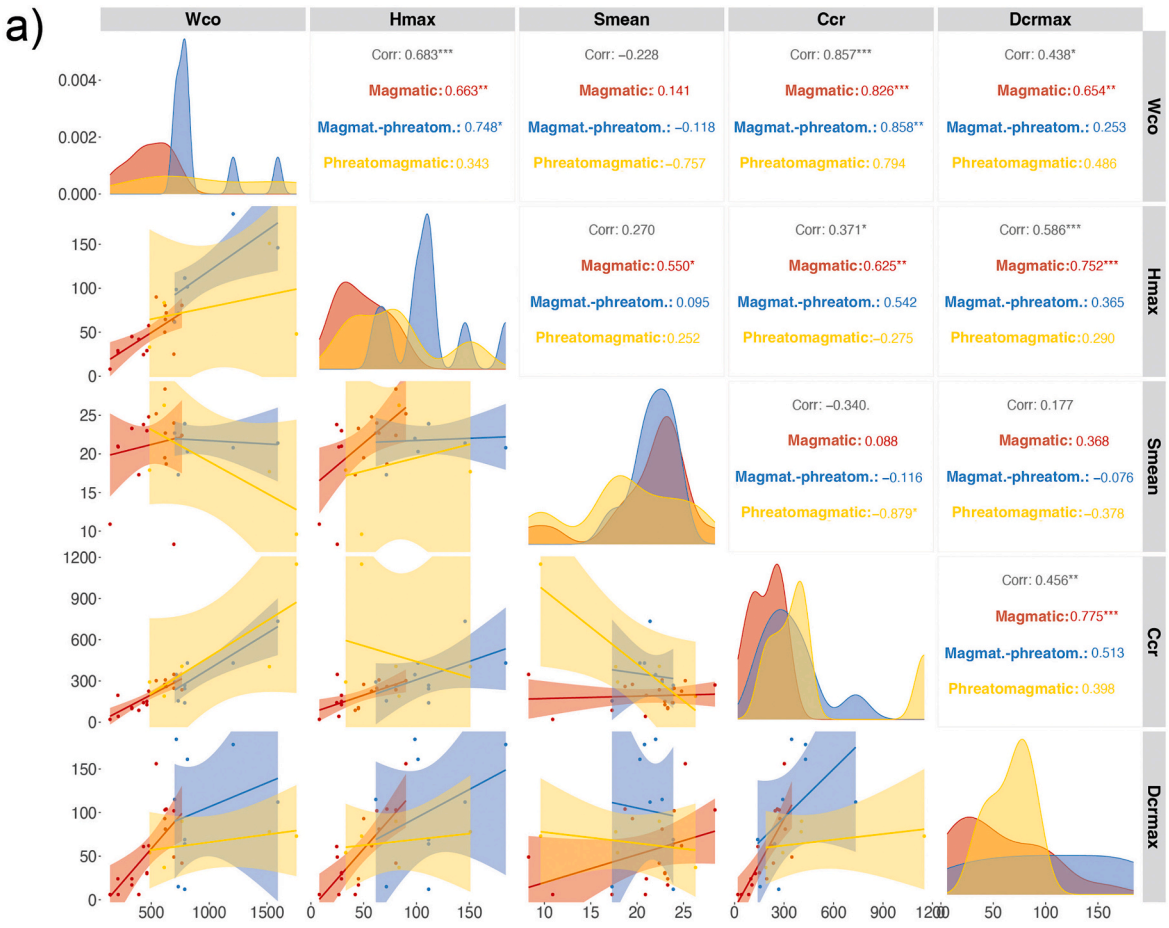

Fig. 13. a) Matrix - scatter plot showing correlations between pairs of morphometric parameters for all three types of edifices described in the GVF (magmatic, magmatic-phreatomagmatic and phreatomagmatic tuff rings-maars); b) biplot of the first two principal components (PC1 and PC2) obtained with the PCA analysis, which explains about 83 % of the cumulative proportion of variance. Black arrows (vectors for each morphometric parameter) indicate relatively strong correlation between maximum crater depth (D_{crmax}) and maximum cone height (H_{max}) and an almost complete lack of correlation between S_{mean} and the mean cone diameter (W_{co}) and the mean crater diameter (C_{cr}). See main text for further details.

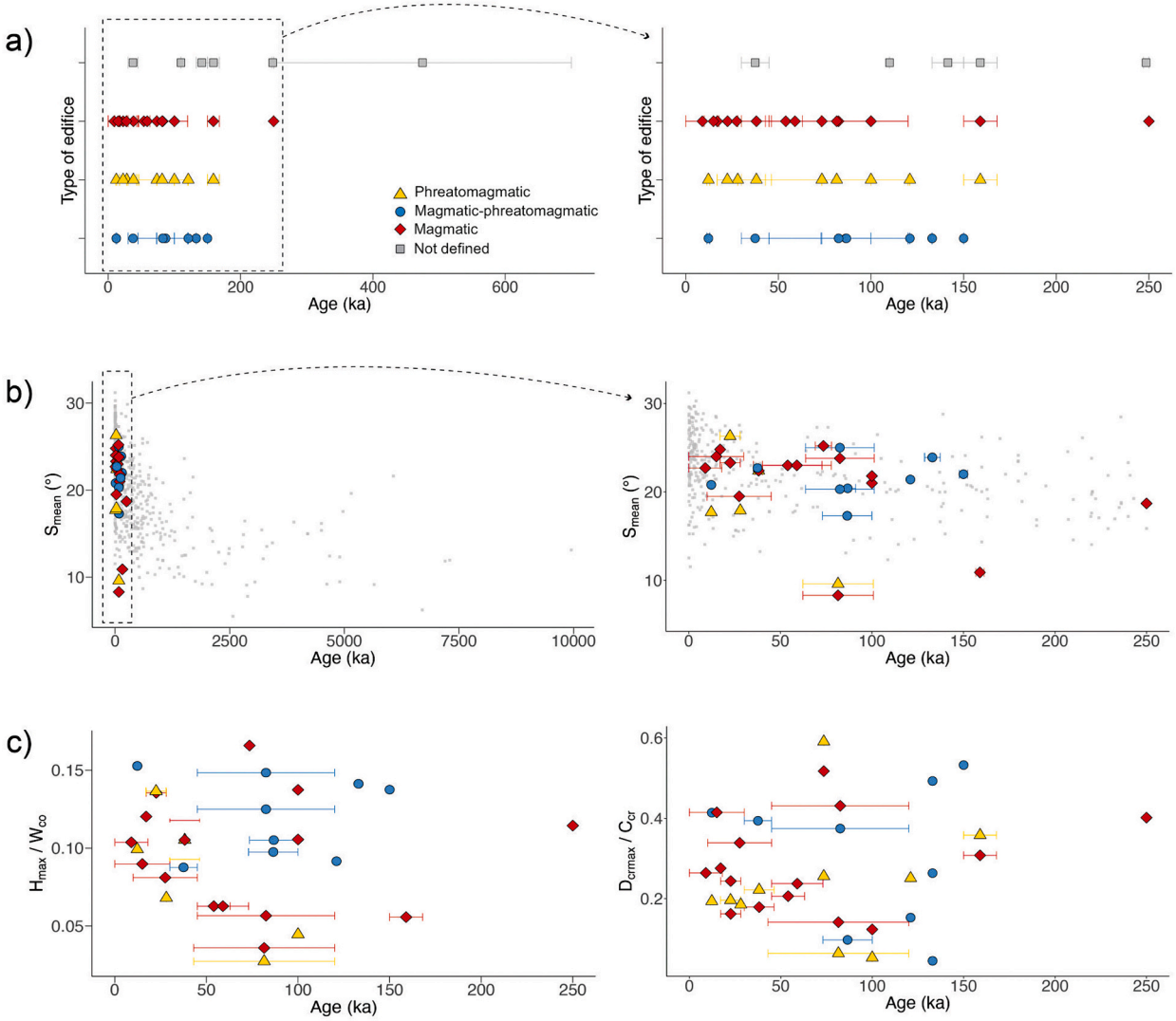

Fig. 14. a) Ages of the different types of volcanic edifices of the GVF based on absolute dating techniques (e.g., C-14, thermoluminescence in plagioclases and sediments, K/Ar, Ar/Ar and U/Th and biostratigraphy) and relative stratigraphy (see: Supp. Material 1); b) age as function of S_{mean} for volcanic edifices located in the GVF and worldwide monogenetic volcanoes (gray squares; Gabor Kereszturi, unpublished data); c) ratio of morphometric parameters vs. age of the GVF volcanic edifices.

are mostly ring-shaped (73 %) (Fig. 4d). About 50 % of magmatic-phreatomagmatic cones and 54 % of tuff rings-maars are situated on flat surfaces, indicating the potential presence of groundwater during eruptions. These flat areas typically consist of softer sediments with more saturated pore spaces. The GVF is notably prone to generating phreatomagmatic eruptions, as evidenced by 50 % of eruptions including a phreatomagmatic phase (Fig. 5). This characteristic underscores the interaction between magma and water during volcanic activity in the region.

In the case of magmatic-phreatomagmatic volcanoes in the GVF, sedimentary evidence indicates varied eruptive sequences. Some volcanoes, such as Sant Marc, Pujalós, and Puig Subià (Fig. 15), show initial phreatomagmatic activity. However, in instances like Montsacopa (Fig. 15), phreatomagmatic deposits formed towards the end of the eruption, a phenomenon less commonly observed in other volcanic fields such as Auckland Volcanic Field in New Zealand (Kereszturi et al., 2014), Bakony-Balaton Highland in Hungary (Martin and Németh, 2004; Kereszturi et al., 2011), Pali Aike Volcanic Field in Argentina, Cile (Mazzarini and D'Orazio, 2003) or Jeju Island, South Korea (Sohn, 1996).

The depletion of magma supply with initial phreatomagmatic activity can influence the final morphology of the volcanoes, by potentially limiting the magma volume available for scoria cone building, as observed by the presence of smaller to medium-sized cones within the GVF (e.g., Pujalós; Figs. 2 and 15). Conversely, in cases like Montsacopa (Figs. 2 and 15), where magma supply remains relatively high, late-stage phreatomagmatic activity has a limited impact on overall cone morphology. These late-stage phases may play a "protective" role by sealing the underlying magmatic deposits with tuff deposits, thereby preserving the shape and integrity of the cone. However, the presence of mantling tuff deposits can alter degradation patterns by affecting surface permeability and promoting overland flow, contrasting with the loose, porous scoria-dominated successions (e.g., Dohrenwend et al., 1986; Wells et al., 1990; Hooper, 1999; Valentine et al., 2006).

In certain instances, the morphometric signatures of magmatic-phreatomagmatic volcanoes resemble those of tuff rings, such as Puig d'Àdri (Table 2 and Fig. 10), rather than the characteristics observed in scoria cones, as seen at Croscat, Aiguanegra o Puig de la Banya de la Boc (Table 2 and Fig. 15). These edifices show higher W_{co}, H_{max} and wider craters (W_{cr}; Supp. Material 1) compared to scoria cones. In this context, the influence of phreatomagmatic phases on the final morphology of these cones is evident, likely widening the craters due to the migration of

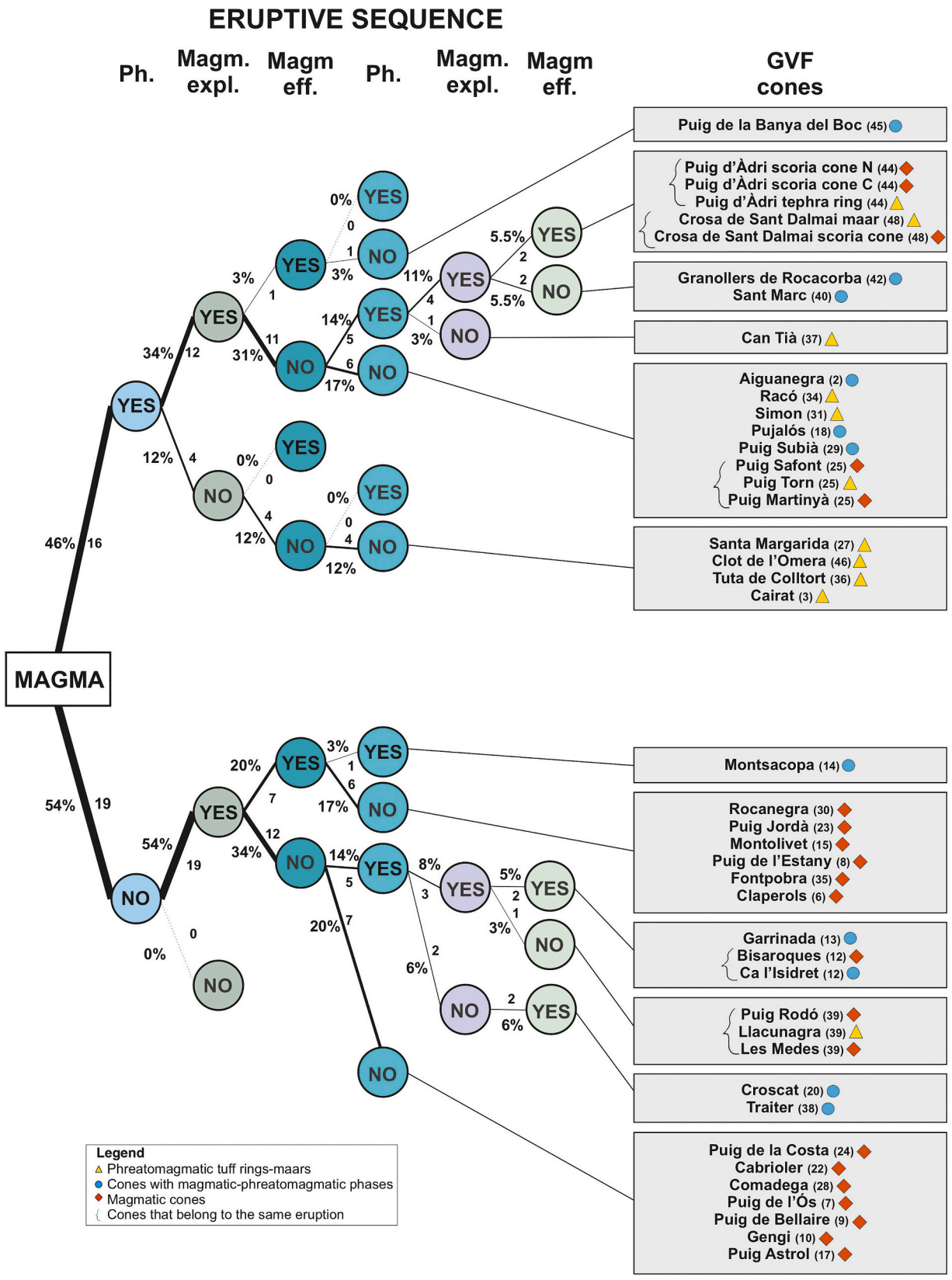

Fig. 15. A binary eruptive sequence tree diagram of the GVF volcanoes. Numbers in parenthesis refer to Fig. 2. The line thicknesses are proportional to the percentage values. ph.—phreatomagmatic phase; magm. expl.-magmatic explosive phase; magm. eff.—magmatic effusive phase.

the fragmentation focus. Phreatomagmatic eruptions typically involve lower fragmentation levels compared to normal Strombolian eruptions (White and Ross, 2011; Valentine et al., 2014).

The largest maars such as La Crosa de Sant Dalmai or Santa Margarida (Fig. 2) exhibit morphological differences compared to other landforms (Fig. 10) including lower values of H_{max}/W_{co} or larger values of C_{cr} and W_{co} (Table 2). Their depositional sequences are characterized by fallout deposits or wet-to-dry PDCs, featuring generally poorly sorted ejecta of juvenile clasts with subordinate amounts of accidental clasts, similar to other tuff rings and maars (Sohn and Chough, 1993; Sohn and Park, 2005; Agustín-Flores et al., 2015; Kshirsagar et al., 2015). Therefore, these distinctive geometries and morphologies are primarily interpreted as the result of specific eruptive processes and deposition mechanisms.

5.2. Relative ages

In this study, morphometric parameters were employed to infer relative chronology within the GVF (Fig. 14). However, the results of the morphometric analysis are insufficient for establishing a precise chronology for the GVF. No significant correlation was observed between edifice type and age (Fig. 14a). While high S_{mean} values were noted in younger volcanoes like Rocanegra, Puig Jordà, Montolivet, and Puig de la Costa (Fig. 2), a general decrease in flank slope with age is only roughly discernible, compared to global datasets (Fig. 14b). This may further indicate little erosional modification of the GVF cones, and underscore the influence of *syn*-eruptive morphometric variability. The bimodal distribution of slope angles (Supp. Material 2) provides evidence for secondary impacts from both syn- and post-emplacement processes on scoria cones in the GVF (Supp. Material 2). This distribution can indicate localized post-eruptive reworking of loose tephra, such as overland flow and debris apron development, and potential variations in grain size and particle cohesion, which can affect factors like the angle of repose and block-to-ash fraction. Directional variability in slope angles (polar plots in Supp. Material 2), H_{max}/W_{co} ratio, and D_{crmax}/C_{cr} (Fig. 14c) further supports this interpretation.

Therefore, the GVF showcases a spectrum of morphological complexities that complicate the inference of relative ages through cone morphometry, highlighting the necessity for cautious interpretation.

5.3. Spatial distribution

The GVF exhibits an uneven spatial distribution of the volcanic landforms, with 84 % of the volcanoes located in the northern sector (Fig. 5). The average vent density is 1.6×10^{-1} vents/km^2, comparable to other monogenetic fields like the Michoacán Volcanic Field in Mexico ($\sim 2.60 \times 10^{-1}$ vents/km^2; Pérez-López et al., 2011) and the Auckland Volcanic Field in New Zealand ($\sim 1.46 \times 10^{-1}$ vents/km^2; Le Corvec et al., 2013). Volcanic landforms in the GVF appear clustered, with a slightly higher density observed in the northern part of the field compared to the south (Fig. 12a).

This distribution is influenced by the interplay of tectonic and magmatic processes, known to shape the distribution of monogenetic volcanoes (e.g., Tibaldi, 1995; Martí et al., 2011; Tadini et al., 2014; Báez et al., 2017).

Approximately half of the cones are of magmatic origin, predominantly situated in the northern part of the GVF (Fig. 12b), alongside the magmatic-phreatomagmatic volcanoes (Fig. 12c). In contrast, phreatomagmatic cones are notably concentrated in the central and southern areas of the field (Fig. 12d).

This spatial distribution aligns with morphometric parameters, where the widest edifices (W_{co}) are primarily located in the southern part (Fig. 11a), and the tallest volcanoes (H_{max}) are concentrated in the northern area (Fig. 11b).

A similar pattern emerges for the crater parameters: the widest craters (C_{cr}) are predominantly found in the southern sector (Fig. 11c), while the deepest craters (D_{cr}) are more prevalent in the northern part (Fig. 11d).

The distribution of phreatomagmatic volcanoes within the GVF is influenced by several sedimentary aquifers spanning the northern and southern sectors including the Eocene formations Cadí-Tavertet, Beuda, Bracons and Folgueroles, and the Quaternary unconsolidated sediments and volcanic deposits. A distinct aquifer is found only in the southern area of the GVF, and it corresponds to the highly fractured (granites and schists) Palaeozoic rocks (Martí et al., 2011; Planagumà et al., 2023).

However, the disparities in eruptive sequences (Fig. 15) and observed morphologies (Figs. 5 and 9) within the GVF cannot be solely attributed to variations in substrate geology or aquifer properties. The spatial pattern of phreatomagmatic eruptions may be explained by fluctuating magma pressures within conduits, influencing the onset and intensity of magma-water interactions during eruptions (Planagumà et al., 2023). These variations in magma discharge rates are critical factors controlling the characteristics of phreatomagmatism (Zimanowski et al., 1997; Zimanowski, 1998; White and Ross, 2011), explosive capacity of erupting magma (Sheridan and Wohletz, 1981) and the emplacements of associated deposits and morphologies such as tuff cones and tuff rings-maars (Kereszturi and Németh, 2012).

Additionally, climatic changes over the past 700,000 years likely altered hydraulic conditions in aquifers, potentially contributing to the variability in magmatic-phreatomagmatic eruptions (Planagumà et al., 2023).

The GVF provides a compelling example of the complexity that characterizes monogenetic volcanism, highlighting how a relatively small area can be characterized by complex eruptive sequences and morphologies.

6. Conclusions

- The monogenetic landforms of the GVF are typified by approximately 50 % magmatic cones, primarily formed through Strombolian eruptions. The remaining 50 % of landforms are evenly divided between magmatic-phreatomagmatic volcanoes and phreatomagmatic tuff rings-maars, where interactions between magma and water played a significant role in driving the fragmentation process.
- The morphometries of the three genetic types overlap without clear distinctions, although in some instances, differences can be noted.
- The data suggest that the morphometric variability observed in the GVF arises from differences in the properties of pyroclastic sequences, such as tephra-dominated versus scoria-dominated deposits. These variations are influenced by diverse eruption styles as well as pre- and post-eruptive factors.
- In the GVF, magmatic and magmatic-phreatomagmatic volcanoes predominantly cluster in the northern part of the field, whereas phreatomagmatic volcanoes are concentrated in the central and southern areas.
- The GVF shows a combination of various eruption styles: 46 % of the identified eruptive sequences exhibit an initial phreatomagmatic activity and in 54 % of eruptions the first phase was predominantly magmatic explosive. Many eruptions demonstrate transitions between these phases.
- Morphology does not strongly correlate with age in the GVF due to the overall youthfulness of its volcanic features and the variability in morphometric characteristics. Therefore, relative chronology cannot be reliably established using morphology alone.

CRediT authorship contribution statement

Dario Pedrazzi: Writing – review & editing, Writing – original draft, Supervision, Software, Methodology, Investigation, Data curation. **Gabor Kereszturi:** Writing – review & editing, Writing – original draft, Methodology, Investigation. **Adelina Geyer:** Writing – review & editing, Writing – original draft, Software, Investigation. **Xavier Bolós:** Writing

– review & editing, Writing – original draft, Investigation. **Jordi Granell:** Writing – review & editing, Writing – original draft, Software, Investigation. **Llorenç Planagumà:** Writing – review & editing, Writing – original draft, Investigation. **Joan Martí:** Writing – review & editing, Writing – original draft. **Daniela Cerda:** Writing – review & editing, Writing – original draft.

Declaration of competing interest

The authors declare that they have no known competing financial interests or personal relationships that could have appeared to influence the work reported in this paper.

Data availability

Data will be made available on request.

Acknowledgments

Dario Pedrazzi is grateful for his Juan de la Cierva (IJCI-2016-30482) contract and his grant Beca d'investigació "Oriol de Bolós" en Ciències Naturals (Ciutat d'Olot 2023, Spain). Xavier Bolós is supported by a fellowship from the Fundación General CSIC's ComFuturo program, which has received funding from the European Union's Horizon 2020 research and innovation programme under the Marie Skłodowska-Curie grant agreement No. 101034263. We are grateful to La Garrotxa Volcanic Zone Natural Park (GVZNP) and its staff for their support throughout this study. We thank the Editor Markus Stoffel, John Smellie and two anonymous referees for their thorough and constructive reviews.

Appendix A. Supplementary material

Supplementary data to this article can be found online at https://doi.org/10.1016/j.geomorph.2024.109400.

References

Aguilera, M., Ureta, G., Grosse, P., Németh, K., Aguilera, F., Vilches, M., 2022. Geomorphological, morphometric, and spatial distribution analysis of the scoria cones in the Negros de Aras monogenetic volcanic field, northern Chile. J. Volcanol. Geotherm. Res. 422 https://doi.org/10.1016/j.jvolgeores.2021.107458.

Agustín-Flores, J., Németh, K., Cronin, S.J., Lindsay, J.M., Kereszturi, G., 2015. Shallow-seated explosions in the construction of the Motukorea tuff ring (Auckland, New Zealand): evidence from lithic and sedimentary characteristics. J. Volcanol. Geotherm. Res. 304 https://doi.org/10.1016/j.jvolgeores.2015.09.013.

Araña, V., Aparicio, A., Martín Escorza, C., Garcia Cacho, L., Ortiz, R., Vaquer Navarro, R., Gassiot, X., 1983. El volcanismo neógeno-cuaternario de Catalunya: caracteres estructurales, petrológicos y geodinámicos.

Báez, W., Carrasco Nuñez, G., Giordano, G., Viramonte, J.G., Chiodi, A., 2017. Polycyclic scoria cones of the Antofagasta de la Sierra basin, Southern Puna plateau, Argentina. Geol. Soc. Spec. Publ. https://doi.org/10.1144/SP446.3.

Barde-Cabusson, S., Bolós, X., Pedrazzi, D., Lovera, R., Serra, G., Martí, J., Casas, A., 2013. Electrical resistivity tomography revealing the internal structure of monogenetic volcanoes. Geophys. Res. Lett. 40 https://doi.org/10.1002/grl.50538.

Barde-Cabusson, S., Gottsmann, J., Martí, J., Bolós, X., Camacho, A.G., Geyer, A., Planagumà, L., Ronchin, E., Sánchez, A., 2014. Structural control of monogenetic volcanism in the Garrotxa volcanic field (Northeastern Spain) from gravity and self-potential measurements. Bull. Volcanol. 76 https://doi.org/10.1007/s00445-013-0788-0.

Bartolini, S., Bolós, X., Martí, J., Pedra, E.R., Planagumà, L., 2015. Hazard assessment at the Quaternary La Garrotxa Volcanic Field (NE Iberia). Nat. Hazards 78. https://doi.org/10.1007/s11069-015-1774-y.

Becerra-Ramírez, R., Dóniz-Páez, J., González, E., 2022. Morphometric analysis of scoria cones to define the 'volcano-type' of the Campo de Calatrava volcanic region (Central Spain). Land 11. https://doi.org/10.3390/land11060917.

Bemis, K.G., Ferencz, M., 2017. Morphometric Analysis of Scoria Cones: The Potential for Inferring Process from Shape. Geological Society Special Publication. https://doi.org/10.1144/SP446.9.

Bemis, K., Walker, J., Borgia, A., Turrin, B., Neri, M., Swisher, C., 2011. The growth and erosion of cinder cones in Guatemala and El Salvador: models and statistics. J. Volcanol. Geotherm. Res. 201 https://doi.org/10.1016/j.jvolgeores.2010.11.007.

Ben-Asher, M., Haviv, I., Roering, J.J., Crouvi, O., 2017. The influence of climate and microclimate (aspect) on soil creep efficiency: cinder cone morphology and evolution along the eastern Mediterranean Golan Heights. Earth Surf. Process. Landf. 42 https://doi.org/10.1002/esp.4214.

Bolós, A., 1925. La Estació paleontològica del" Pont de Ferro" i algunes consideracions sobre el volcanisme Olotí. Butlletí la Inst. Catalana d'Història Nat. 112–120.

Bolós, X., Barde-Cabusson, S., Pedrazzi, D., Martí, J., Casas, A., Himi, M., Lovera, R., 2012. Investigation of the inner structure of La Crosa de Sant Dalmai maar (Catalan volcanic zone, Spain). J. Volcanol. Geotherm. Res. 247, 37–48.

Bolós, X., Barde-Cabusson, S., Pedrazzi, D., Martí, J., Casas, A., Lovera, R., Nadal-Sala, D., 2014a. Geophysical exploration on the subsurface geology of La Garrotxa monogenetic volcanic field (NE Iberian Peninsula). Int. J. Earth Sci. 103 https://doi.org/10.1007/s00531-014-1044-3.

Bolós, X., Planagumà, L., Martí, J., 2014b. Volcanic stratigraphy of the Quaternary La Garrotxa Volcanic Field (north-east Iberian Peninsula). J. Quat. Sci. 29 https://doi.org/10.1002/jqs.2725.

Bolós, X., Martí, J., Becerril, L., Planagumà, L., Grosse, P., Barde-Cabusson, S., 2015. Volcano-structural analysis of La Garrotxa Volcanic Field (NE Iberia): implications for the plumbing system. Tectonophysics 642. https://doi.org/10.1016/j.tecto.2014.12.013.

Breed, W.J., 1964. Morphology and lineation of cinder cones in the San Francisco Volcanic Field. Mus. North. Ariz. Bull. 40, 65–71.

Burjachs, F., 1985. Aplicació de l'ànalisi pol· línica al jaciment arqueològic de la Cova 120 (Alta Garrotxa, Catalunya). Fac. Lletres, Univ. Autònoma Barcelona. Bellaterra. Tesis Licenciatura.

Büttner, R., Zimanowski, B., 1998. Physics of thermohydraulic explosions. Phys. Rev. E - Stat. Physics, Plasmas, Fluids, Relat. Interdiscip. Top. 57 https://doi.org/10.1103/PhysRevE.57.5726.

Cebrià, J.M., López-Ruiz, J., Doblas, M., Oyarzun, R., Hertogen, J., Benito, R., 2000. Geochemistry of the Quaternary alkali basalts of Garrotxa (NE Volcanic Province, Spain): a case of double enrichment of the mantle lithosphere. J. Volcanol. Geotherm. Res. 102 https://doi.org/10.1016/S0377-0273(00)00189-X.

Cimarelli, C., Di Traglia, F., de Rita, D., Gimeno Torrente, D., Fernandez Turiel, J.L., 2013. Space-time evolution of monogenetic volcanism in the mafic Garrotxa Volcanic Field (NE Iberian Peninsula). Bull. Volcanol. 75 https://doi.org/10.1007/s00445-013-0758-6.

Colton, H.S., 1937. The basaltic cinder cones and lava flows of the San Francisco Mountain volcanic field. Mus. North. Ariz. Bull. 10, 1–49.

Connor, C.B., Connor, L., Germa, A., Richardson, J., Bebbington, M., Gallant, E., Saballos, A., 2019. How to use kernel density estimation as a diagnostic and forecasting tool for distributed volcanic vents. Stat. Volcanol. 4 https://doi.org/10.5038/2163-338x.4.3.

Corazzato, C., Tibaldi, A., 2006. Fracture control on type, morphology and distribution of parasitic volcanic cones: an example from Mt. Etna, Italy. J. Volcanol. Geotherm. Res. 158 https://doi.org/10.1016/j.jvolgeores.2006.04.018.

Delcamp, A., van Wyk de Vries, B., Stéphane, P., Kervyn, M., 2014. Endogenous and exogenous growth of the monogenetic Lemptégy volcano, Chaîne des Puys, France. Geosphere 10. https://doi.org/10.1130/GES01007.1.

Di Traglia, F., Cimarelli, C., de Rita, D., Gimeno Torrente, D., 2009. Changing eruptive styles in basaltic explosive volcanism: examples from Croscat complex scoria cone, Garrotxa Volcanic Field (NE Iberian Peninsula). J. Volcanol. Geotherm. Res. 180 https://doi.org/10.1016/j.jvolgeores.2008.10.020.

Dohrenwend, J.C., Wells, S.G., Turrin, B.D., 1986. Degradation of Quaternary cinder cones in the Cima volcanic field, Mojave Desert, California. Geol. Soc. Am. Bull. 97 https://doi.org/10.1130/0016-7606(1986)97<421:DOQCCI>2.0.CO;2.

Dóniz, J., Romero, C., Carmona, J., García, A., 2011. Erosion of cinder cones in Tenerife by gully formation, Canary Islands, Spain. Phys. Geogr. 32 https://doi.org/10.2747/0272-3646.32.2.139.

Dóniz-Páez, F.J., 2001. La influencia de la topografía en las características morfológicas y morfométricas de los volcanes basálticos monogénicos de Tenerife (Islas Canarias). Cuaternario y Geomorfol. Rev. la Soc. Española Geomorfol. y Asoc. Española para el Estud. del Cuaternario 15, 125–129.

Dóniz-Páez, J., 2015. Volcanic geomorphological classification of the cinder cones of Tenerife (Canary Islands, Spain). Geomorphology 228. https://doi.org/10.1016/j.geomorph.2014.10.004.

Donville, B., 1973. Ages potassium-argon des vulcanites du Haut-Ampurdan (Nord-Est de l'Espagne). Implications stratigraphiques. C.R. ACAD. SCI., D; FR. 276, 0018. P. 2497 A 2500. https://pascal-francis.inist.fr/vibad/index.php?action=getRecordDetail&idt=PASCALGEODEBRGM732222119.

Favalli, M., Karátson, D., Mazzarini, F., Pareschi, M.T., Boschi, E., 2009. Morphometry of scoria cones located on a volcano flank: a case study from Mt. Etna (Italy), based on high-resolution LiDAR data. J. Volcanol. Geotherm. Res. 186 https://doi.org/10.1016/j.jvolgeores.2009.07.011.

Fornaciai, A., Favalli, M., Karátson, D., Tarquini, S., Boschi, E., 2012. Morphometry of scoria cones, and their relation to geodynamic setting: a DEM-based analysis. J. Volcanol. Geotherm. Res. 217–218 https://doi.org/10.1016/j.jvolgeores.2011.12.012.

Galán, G., Cruz, E., Fernández-Roig, M., Martínez, F.J., Oliveras, V., 2016. Mineral associations and major element compositions of base metal sulphides from the subcontinental lithospheric mantle of NE Spain. Mineral. Petrol. 110 https://doi.org/10.1007/s00710-015-0415-1.

Gisbert, G., Gimeno, D., Fernandez-Turiel, J.L., 2009. Eruptive mechanisms of the Puig De La Garrinada volcano (Olot, Garrotxa volcanic field, Northeastern Spain): a methodological study based on proximal pyroclastic deposits. J. Volcanol. Geotherm. Res. 180 https://doi.org/10.1016/j.jvolgeores.2008.12.018.

Graettinger, A.H., 2018. Trends in maar crater size and shape using the global Maar Volcano Location and Shape (MaarVLS) database. J. Volcanol. Geotherm. Res. 357, 1–13.

Grosse, P., Ochi Ramacciotti, M.L., Escalante Fochi, F., Guzmán, S., Orihashi, Y., Sumino, H., 2020. Geomorphology, morphometry, spatial distribution and ages of mafic monogenetic volcanoes of the Peinado and Incahuasi fields, southernmost Central Volcanic Zone of the Andes. J. Volcanol. Geotherm. Res. 401 https://doi.org/10.1016/j.jvolgeores.2020.106966.

Guérin, G., Valladas, G., 1980. Thermoluminescence dating of volcanic plagioclases. Nature 286. https://doi.org/10.1038/286697a0.

Guérin, G., Behamoun, G., Mallarach, J.M., 1985. Un exemple de fusió parcial en medi continental. El vulcanisme quaternari de la Garrotxa. Publicació del Mus. Comarc. la Garrotxa 1, 19–26.

Guilbaud, M.N., Siebe, C., Layer, P., Salinas, S., Castro-Govea, R., Garduño-Monroy, V.H., Le Corvec, N., 2011. Geology, geochronology, and tectonic setting of the Jorullo Volcano region, Michoacán, México. J. Volcanol. Geotherm. Res. 201 https://doi.org/10.1016/j.jvolgeores.2010.09.005.

Haag, M.B., Baez, W.A., Sommer, C.A., Arnosio, J.M., Filipovich, R.E., 2019. Geomorphology and spatial distribution of monogenetic volcanoes in the southern Puna Plateau (NW Argentina). Geomorphology 342. https://doi.org/10.1016/j.geomorph.2019.06.008.

Hooper, D.M., 1999. Cinder movement experiments on scoria cones slopes: rates and direction of transport. Landf. Anal. 2, 5–18.

Iriarte, E., Revelles, J., Finsinger, W., Mesquita-Joanes, F., Rodrigo, M.A., Burjachs, F., Expósito, I., Marti Molist, J., Planagumà, L., Alcalde, G., Saña, M., 2023. Youngest Iberian Holocene volcanic eruptions and paleoenvironmental evolution of a barrier-paleolake in the Garrotxa Volcanic Field (NE Spain). Holocene 33. https://doi.org/10.1177/09596836231169989.

Kereszturi, G., Németh, K., 2012. Monogenetic basaltic volcanoes: genetic classification, growth, geomorphology and degradation. In: Updates in Volcanology - New Advances in Understanding Volcanic Systems. https://doi.org/10.5772/51387.

Kereszturi, G., Németh, K., 2016. Sedimentology, eruptive mechanism and facies architecture of basaltic scoria cones from the Auckland Volcanic Field (New Zealand). J. Volcanol. Geotherm. Res. 324 https://doi.org/10.1016/j.jvolgeores.2016.05.012.

Kereszturi, G., Németh, K., Csillag, G., Balogh, K., Kovács, J., 2011. The role of external environmental factors in changing eruption styles of monogenetic volcanoes in a Mio/Pleistocene continental volcanic field in western Hungary. J. Volcanol. Geotherm. Res. 201, 227–240.

Kereszturi, G., Jordan, G., Németh, K., Dóniz-Páez, J.F., 2012. Syn-eruptive morphometric variability of monogenetic scoria cones. Bull. Volcanol. 74 https://doi.org/10.1007/s00445-012-0658-1.

Kereszturi, G., Geyer, A., Martí, J., Németh, K., Dóniz-Páez, F.J., 2013. Evaluation of morphometry-based dating of monogenetic volcanoes-a case study from Bandas del Sur, Tenerife (Canary Islands). Bull. Volcanol. 75 https://doi.org/10.1007/s00445-013-0734-1.

Kereszturi, G., Németh, K., Cronin, S.J., Procter, J., Agustín-Flores, J., 2014. Influences on the variability of eruption sequences and style transitions in the Auckland Volcanic Field, New Zealand. J. Volcanol. Geotherm. Res. 286 https://doi.org/10.1016/j.jvolgeores.2014.09.002.

Kervyn, M., Ernst, G.G.J., Carracedo, J.C., Jacobs, P., 2012. Geomorphometric variability of "monogenetic" volcanic cones: evidence from Mauna Kea, Lanzarote and experimental cones. Geomorphology 136. https://doi.org/10.1016/j.geomorph.2011.04.009.

Kshirsagar, P., Siebe, C., Guilbaud, M.N., Salinas, S., Layer, P.W., 2015. Late Pleistocene Alberca de Guadalupe maar volcano (Zacapu basin, Michoacán): Stratigraphy, tectonic setting, and paleo-hydrogeological environment. J. Volcanol. Geotherm. Res. 304 https://doi.org/10.1016/j.jvolgeores.2015.09.003.

Kurszlaukis, S., Lorenz, V., 2017. Differences and Similarities between Emplacement Models of Kimberlite and Basaltic Maar-Diatreme Volcanoes. Geological Society Special Publication. https://doi.org/10.1144/SP446.5.

Le Corvec, N., Bebbington, M.S., Lindsay, J.M., McGee, L.E., 2013. Age, distance, and geochemical evolution within a monogenetic volcanic field: analyzing patterns in the Auckland Volcanic Field eruption sequence. Geochem. Geophys. Geosyst. 14 https://doi.org/10.1002/ggge.20223.

Lewis, C.J., Vergés, J., Marzo, M., 2000. High mountains in a zone of extended crust: Insights into the Neogene-Quaternary topographic development of northeastern Iberia. Tectonics 19. https://doi.org/10.1029/1999TC900056.

López Ruiz, J., Rodríguez Badiola, E., 1985. La región volcánica mio-pleistocena del NE de España. Estud. Geol. 41 https://doi.org/10.3989/egeol.85413-4696.

Losantos, M., Planagumà, L.L., Bassols, E., Pijuan, J., de Paz, A., Berástegui, X., 2007. Carta vulcanològica de la zona volcànica de la Garrotxa.

Mallarach, J.M., 1982. Carta geologica de la regió volcanica d'Olot. Litol. i Geomorfol. 1120.

Mallarach i Carrera, J.M., 1998. El vulcanisme prehistòric de Catalunya. Diputació de Girona.

Mallarach, J.M., Riera, M., 1981. Els volcans olotins i el seu paisatge. Serpa, Barcelona.

Martí, J., 2000. El vulcanisme: Guia de camp de la Zona Volcànica de la Garrotxa. Generalitat de Catalunya, Departament de Medi Ambient.

Martí, J., Bolós, X., 2019. The Neogene-Quaternary Alkaline Volcanism of Iberia. https://doi.org/10.1007/978-3-030-11190-8_6.

Martí, J., Mallarach, J.M., 1987. Erupciones hidromagmáticas en el volcanismo cuaternario de Olot (Girona). Estud. Geol. 43 https://doi.org/10.3989/egeol.87431-2568.

Martí, J., Ortiz, R., Claudin, F., Mallarach, J., 1986. Mecanismos eruptivos del volcán de la closa de San Dalmai (Girona). An. física. Ser. B, Apl. métodos e instrumentos 82, 143–153.

Martí, J., Mitjavila, J., Roca, E., Aparicio, A., 1992. Cenozoic magmatism of the valencia trough (western mediterranean): relationship between structural evolution and volcanism*. Tectonophysics 203. https://doi.org/10.1016/0040-1951(92)90221-Q.

Martí, J., Planagumà, L., Geyer, A., Canal, E., Pedrazzi, D., 2011. Complex interaction between Strombolian and phreatomagmatic eruptions in the Quaternary monogenetic volcanism of the Catalan Volcanic Zone (NE of Spain). J. Volcanol. Geotherm. Res. 201 https://doi.org/10.1016/j.jvolgeores.2010.12.009.

Martí, J., Planagumà, L., Geyer, A., Aguirre-Díaz, G., Pedrazzi, D., Bolós, X., 2017. Basaltic ignimbrites in monogenetic volcanism: the example of La Garrotxa volcanic field. Bull. Volcanol. 79 https://doi.org/10.1007/s00445-017-1113-0.

Martin, U., Németh, K., 2004. Mio/Pliocene Phreatomagmatic Volcanism in the Western Pannonian Basin. Geological Institute of Hungary.

Mazzarini, F., D'Orazio, M., 2003. Spatial distribution of cones and satellite-detected lineaments in the Pali Aike Volcanic Field (southernmost Patagonia): Insights into the tectonic setting of a Neogene rift system. J. Volcanol. Geotherm. Res. 125 https://doi.org/10.1016/S0377-0273(03)00120-3.

Mazzarini, F., Le Corvec, N., Isola, I., Favalli, M., 2016. Volcanic field elongation, vent distribution, and tectonic evolution of a continental rift: the Main Ethiopian Rift example. Geosphere 12. https://doi.org/10.1130/GES01193.1.

McGetchin, T.R., Settle, M., Chouet, B.A., 1974. Cinder cone growth modeled after Northeast Crater, Mount Etna, Sicily. J. Geophys. Res. 79 https://doi.org/10.1029/jb079i023p03257.

Miranda-Muruzábal, M., Geyer, A., Aulinas, M., Albert, H., Vilà, M., Micheo, F., Bolós, X., Pedrazzi, D., Gisbert, G., Planagumà, L., 2024. CatVolc: a new database of geochemical and geochronological data of volcanic-related materials from the Catalan Volcanic Zone (Spain). J. Volcanol. Geotherm. Res. 446, 107998.

Murcia, H., Németh, K., 2020. Effusive monogenetic volcanism. In: Updates in Volcanology - Transdisciplinary Nature of Volcano Science. https://doi.org/10.5772/intechopen.94387.

Németh, K., Kereszturi, G., 2015. Monogenetic volcanism: personal views and discussion. Int. J. Earth Sci. 104 https://doi.org/10.1007/s00531-015-1243-6.

Neumann, E.R., Martí, J., Mitjavila, J., Wulff-Pedersen, E., 1999. Origin and implications of mafic xenoliths associated with Cenozoic extension-related volcanism in the València Trough, NE Spain. Mineral. Petrol. 65 https://doi.org/10.1007/BF01161579.

Nieto-Torres, A., Del Pozzo, A.L.M., 2019. Spatio-temporal hazard assessment of a monogenetic volcanic field, near México City. J. Volcanol. Geotherm. Res. 371 https://doi.org/10.1016/j.jvolgeores.2019.01.006.

Pedersen, G.B.M., 2016. Semi-automatic classification of glaciovolcanic landforms: an object-based mapping approach based on geomorphometry. J. Volcanol. Geotherm. Res. 311 https://doi.org/10.1016/j.jvolgeores.2015.12.015.

Pedersen, G.B.M., Grosse, P., Gudmundsson, M.T., 2020. Morphometry of glaciovolcanic edifices from Iceland: types and evolution. Geomorphology 370. https://doi.org/10.1016/j.geomorph.2020.107334.

Pedrazzi, D., Bolós, X., Martí, J., 2014. Phreatomagmatic volcanism in complex hydrogeological environments: La crosa de sant dalmai maar (Catalan Volcanic Zone, NE Spain). Geosphere 10. https://doi.org/10.1130/GES00959.1.

Pedrazzi, D., Bolós, X., Barde-Cabusson, S., Martí, J., 2016. Reconstructing the eruptive history of a monogenetic volcano through a combination of fieldwork and geophysical surveys: the example of Puig d'Àdri (Garrotxa Volcanic Field). J. Geol. Soc. Lond. 173 https://doi.org/10.1144/jgs2016-009.

Pedrazzi, D., Kereszturi, G., Lobo, A., Geyer, A., Calle, J., 2020. Geomorphology of the post-caldera monogenetic volcanoes at Deception Island, Antarctica — implications for landform recognition and volcanic hazard assessment. J. Volcanol. Geotherm. Res. 402 https://doi.org/10.1016/j.jvolgeores.2020.106986.

Pedrazzi, D., Cerda, D., Geyer, A., Martí, J., Aulinas, M., Planagumà, L., 2022. Stratigraphy and eruptive history of the complex Puig de La Banya del Boc monogenetic volcano, Garrotxa Volcanic Field. J. Volcanol. Geotherm. Res. 423 https://doi.org/10.1016/j.jvolgeores.2021.107460.

Pérez-López, R., Legrand, D., Garduño-Monroy, V.H., Rodríguez-Pascua, M.A., Giner-Robles, J.L., 2011. Scaling laws of the size-distribution of monogenetic volcanoes within the Michoacán-Guanajuato Volcanic Field (Mexico). J. Volcanol. Geotherm. Res. 201 https://doi.org/10.1016/j.jvolgeores.2010.09.006.

Planagumà, L., Bolós, X., Martí, J., 2023. Hydrogeologic and magmatic controls on phreatomagmatism at the La Garrotxa monogenetic volcanic field (NE of Iberian Peninsula). J. Volcanol. Geotherm. Res. 441 https://doi.org/10.1016/j.jvolgeores.2023.107894.

Porter, S.C., 1972. Distribution, morphology, and size frequency of cinder cones on mauna kea volcano, Hawaii. Bull. Geol. Soc. Am. 83 https://doi.org/10.1130/0016-7606(1972)83[3607:DMASFO]2.0.CO;2.

Puiguriguer, M., Alcalde, G., Bassols, E., Burjachs, F., Expósito, I., Planagumà, L.L., Saña, M., Yll, E., 2012. 14C dating of the last Croscat volcano eruption (Garrotxa region, NE Iberian Peninsula). Geol. Acta 10. https://doi.org/10.1344/105.000001709.

R Core Team, R, 2020. R: A Language and Environment for Statistical Computing.

Riedel, C., Ernst, G.G.J., Riley, M., 2003. Controls on the growth and geometry of pyroclastic constructs. J. Volcanol. Geotherm. Res. 127 https://doi.org/10.1016/S0377-0273(03)00196-3.

Roqué, C., Linares, R., Zarroca, M., Pallí, L., 2014. The Olot Volcanic Field, in: World Geomorphological Landscapes. https://doi.org/10.1007/978-94-017-8628-7_21.

Schonwalder-Angel, D., Cortés, J.A., Calder, E.S., 2018. The interplay of magmatism and tectonics: an example based on the satellite scoria cones at Llaima volcano, Chile. J. Volcanol. Geotherm. Res. 367 https://doi.org/10.1016/j.jvolgeores.2018.10.020.

Settle, M., 1979. The structure and emplacement of cinder cone fields. Am. J. Sci. 279, 1089–1107.

Sheridan, M.F., Wohletz, K.H., 1981. Hydrovolcanic explosions: the systematics of water-pyroclast equilibration. Science 80 (212), 1387–1389.
Smellie, J.L., Kraus, S., Williams, K., 2023. The 1821 eruption of Bridgeman Island, South Shetland Islands, Antarctica: an observed Capelinhos-style hydrovolcanic event. Antarct. Sci. https://doi.org/10.1017/S0954102023000111.
Sohn, Y.K., 1996. Hydrovolcanic processes forming basaltic tuff rings and cones on Cheju Island, Korea. Bull. Geol. Soc. Am. 108 https://doi.org/10.1130/0016-7606(1996)108<1199:HPFBTR>2.3.CO;2.
Sohn, Y.K., Chough, S.K., 1993. The Udo tuff cone, Cheju Island, South Korea: transformation of pyroclastic fall into debris fall and grain flow on a steep volcanic cone slope. Sedimentology 40. https://doi.org/10.1111/j.1365-3091.1993.tb01359.x.
Sohn, Y.K., Park, K.H., 2005. Composite tuff ring/cone complexes in Jeju Island, Korea: possible consequences of substrate collapse and vent migration. J. Volcanol. Geotherm. Res. 141 https://doi.org/10.1016/j.jvolgeores.2004.10.003.
Tadini, A., Bonali, F.L., Corazzato, C., Cortés, J.A., Tibaldi, A., Valentine, G.A., 2014. Spatial distribution and structural analysis of vents in the lunar crater volcanic field (Nevada, USA). Bull. Volcanol. 76 https://doi.org/10.1007/s00445-014-0877-8.
Thouret, J.C., 1999. Volcanic geomorphology-an overview. Earth Sci. Rev. 47 https://doi.org/10.1016/S0012-8252(99)00014-8.
Tibaldi, A., 1995. Morphology of pyroclastic cones and tectonics. J. Geophys. Res. 100 https://doi.org/10.1029/95jb02250.
Uslular, G., Le Corvec, N., Mazzarini, F., Legrand, D., Gençalioğlu-Kuşcu, G., 2021. Morphological and multivariate statistical analysis of quaternary monogenetic vents in the Central Anatolian Volcanic Province (Turkey): implications for the volcano-tectonic evolution. J. Volcanol. Geotherm. Res. 416 https://doi.org/10.1016/j.jvolgeores.2021.107280.
Valentine, G.A., Connor, C.B., 2015. Basaltic volcanic fields. In: The Encyclopedia of Volcanoes. Elsevier, pp. 423–439.
Valentine, G.A., Perry, F.V., Krier, D., Keating, G.N., Kelley, R.E., Cogbill, A.H., 2006. Small-volume basaltic volcanoes: Eruptive products and processes, and posteruptive geomorphic evolution in Crater Flat (Pleistocene), southern Nevada. Bull. Geol. Soc. Am. 118 https://doi.org/10.1130/B25956.1.
Valentine, G.A., Graettinger, A.H., Sonder, I., 2014. Explosion depths for phreatomagmatic eruptions. Geophys. Res. Lett. 41 https://doi.org/10.1002/2014GL060096.
Vespermann, D., Schmincke, H.-U., 2000. Scoria Cones and Tuff Rings. Academic press.
Wells, S.G., McFadden, L.D., Renault, C.E., Crowe, B.M., 1990. Geomorphic assessment of late Quaternary volcanism in the Yucca Mountain area, southern Nevada: Implications for the proposed high-level radioactive waste repository. Geology 18. https://doi.org/10.1130/0091-7613(1990)018<0549:GAOLQV>2.3.CO;2.
White, J.D.L., Ross, P.S., 2011. Maar-diatreme volcanoes: a review. J. Volcanol. Geotherm. Res. https://doi.org/10.1016/j.jvolgeores.2011.01.010.
Wohletz, K.H., 1986. Explosive magma-water interactions: thermodynamics, explosion mechanisms, and field studies. Bull. Volcanol. 48 https://doi.org/10.1007/BF01081754.
Wood, C.A., 1979. Monogenetic volcanoes of the terrestrial planets. In: Lunar Planet. Sci. Conf. 10th, Proc. v. 3, Plan.
Wood, C.A., 1980a. Morphometric analysis of cinder cone degradation. J. Volcanol. Geotherm. Res. 8 https://doi.org/10.1016/0377-0273(80)90101-8.
Wood, C.A., 1980b. Morphometric evolution of cinder cones. J. Volcanol. Geotherm. Res. 7 https://doi.org/10.1016/0377-0273(80)90040-2.
Zarazúa-Carbajal, M.C., Valentine, G.A., De la Cruz-Reyna, S., 2024. Scoria cone erosional degradation by incision: different behaviors in three volcanic fields reflect environmental conditions. Geology 52 (7), 565–569. https://doi.org/10.1130/G52113.1.
Ziegler, P.A., 1992. European Cenozoic rift system. Tectonophysics 208, 91–111.
Zimanowski, B., 1998. Phreatomagmatic Explosions. From Magma to Tephra, 4. Elsevier, Amsterdam, pp. 25–53.
Zimanowski, B., Büttner, R., Lorenz, V., Häfele, H.G., 1997. Fragmentation of basaltic melt in the course of explosive volcanism. J. Geophys. Res. Solid Earth 102. https://doi.org/10.1029/96jb02935.